ISSN 1991-1696

SAIEE

Africa Research Journal

Research Journal of the South African Institute of Electrical Engineers

Incorporating the SAIEE Transactions

www.saiee.org.za

March 2016
Volume 107 No. 1

SAIEE AFRICA RESEARCH JOURNAL

(SAIEE FOUNDED JUNE 1909 INCORPORATED DECEMBER 1909)
AN OFFICIAL JOURNAL OF THE INSTITUTE
ISSN 1991-1696

Secretary and Head Office
Mrs Gerda Geyer
South African Institute for Electrical Engineers (SAIEE)
PO Box 751253, Gardenview, 2047, South Africa
Tel: (27-11) 487-3003
Fax: (27-11) 487-3002
E-mail: researchjournal@saiee.org.za

Published by
South African Institute of Electrical Engineers (Pty) Ltd, PO Box 751253, Gardenview, 2047
Tel. (27-11) 487-3003, Fax. (27-11) 487-3002,
E-mail: researchjournal@saiee.org.za

Additional reviewers are approached as necessary

ARTICLES SUBMITTED TO THE SAIEE AFRICA RESEARCH JOURNAL ARE FULLY PEER REVIEWED PRIOR TO ACCEPTANCE FOR PUBLICATION

The following organisations have listed SAIEE Africa Research Journal for abstraction purposes:

INSPEC (The Institution of Electrical Engineers, London); 'The Engineering Index' (Engineering Information Inc.)

VOL 107 No 1
March 2016

SAIEE Africa Research Journal

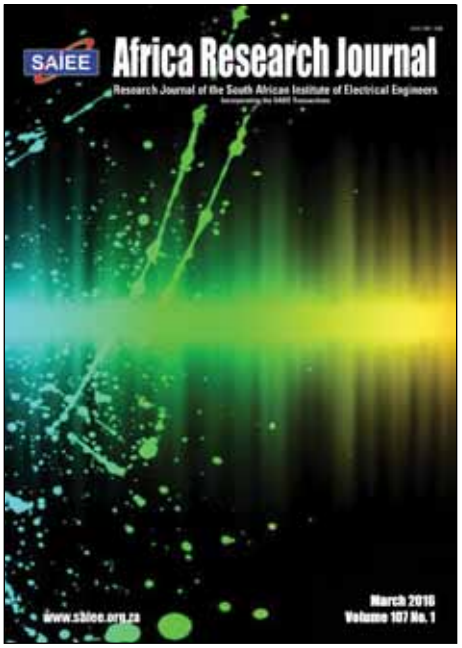

SAIEE AFRICA RESEARCH JOURNAL EDITORIAL STAFF ..... IFC

Modernising, Upgrading and Recommissioning the Indoor Antenna Range at Stellenbosch University 4
D. M. P. Smith, D. B. Davidson, A. Bester and J. Andriambeloson

30-Second and One-Minute Rainfall Rate Modelling and Conversion for Millimetric Wave Propagation in South Africa 17
M. N. Ahuna, T. J. Afullo and A.A. Alonge

Log-domain Interactive Sphere Decoder with Symbol Sorting ... 30
P. R. Botha and B. T. J. (Sunil) Maharaj

Effect of Surface Discharges on Lightning Impulse Breakdown Voltage of Oil-Impregnated Pressboard in Power Transformers 38
M. M. Tshivhilinge and C. Nyamupangedengu

MODERNISING, UPGRADING AND RECOMMISSIONING THE INDOOR ANTENNA RANGE AT STELLENBOSCH UNIVERSITY

D. M. P. Smith*, D. B. Davidson*, A. Bester* and J. Andriambeloson*

* *Department of Electrical and Electronic Engineering, Stellenbosch University, Stellenbosch 7600, South Africa. Email: davidson@sun.ac.za*

Abstract: This paper describes the upgrade to the indoor antenna range at Stellenbosch University. The previous measurement process relied upon obsolescent control equipment and undocumented software; it was critical that these be replaced. Now, the antenna range supports three measurement types using a commercial integrated measurement control system that provides support for high gain and low gain antennas over a wide frequency range. These are spherical near-field, planar near-field and conventional far-field measurements, with the potential to implement cylindrical near-field. The antenna range potentially supports operations from 1 GHz up to 26.5 GHz, though the currently available probes do not cover the full band. The main physical upgrade was performed during October 2014, though investigations had already begun in 2011, and some supplementary tasks were still ongoing at the time of writing. Several innovative commissioning tests have been undertaken, some of which are only possible with near-field metrology, and these are described in the paper.

Key words: Indoor Antenna Range, Spherical Near-Field Measurements, Planar Near-Field Measurements, Far-Field Measurements

1. INTRODUCTION

Stellenbosch University's antenna range was originally built over twenty five years ago under the direction of Prof J. H. Cloete, with the majority of components designed and manufactured internally by members of staff [1]. At around much the same time, a number of other antenna ranges were built in South Africa, including the indoor range at the Pretoria campus of the Council for Scientific and Industrial Research [2], the compact range at Pretoria University [3], and the outdoor range at Paardefontein [4].

This reflected major interest in antenna engineering at the time, which was driven largely, although not exclusively, by defence applications. All of these antenna ranges have provided excellent service over many years to the antenna engineering community in South Africa. Also, they have proven very attractive to overseas companies, particularly the outdoor range at Paardefontein. Recently, the national focus on the Square Kilometre Array radio telescope has given renewed impetus to antenna engineering [5].

Stellenbosch University's facility originally comprised a polarisation axis rotator mounted on an automated planar scanner and cylindrical axis rotator mounted on a manual translation track that permitted these measurement types: cylindrical near-field (CNF), planar near-field (PNF), and far-field (FF) cuts. While this facility was still functional, major components were no longer supported nor properly understood, hindering continual support of this facility. Firstly, the facility relied upon a venerable HP 8510 vector network analyser (VNA), which has not been supported by the manufacturer for several years (originally Hewlett Packard, then Agilent, presently Keysight Technologies). Also, the control equipment relied upon obsolete software, that was effectively undocumented, and legacy drivers. Finally, a number of crucial components were no longer supported, such as the controller for the stepper motors.

With commercial simulation software readily available, it is now the ability to make high quality measurements that differentiates leading research institutes in the field. Access to these facilities is limited, due to the expense of RF measurement equipment, and specialist operators are required to obtain the best results. During the lifespan of this facility to date, well over two hundred post graduate students have been able to receive training at the facility, providing a number of them with a crucial component in their research. This facility is also used in the final year course on high frequency systems. These considerations made modernising and upgrading the facility a priority.

Near-field (NF) metrology has several advantages over FF metrology, with the most obvious being that the probe is not constrained to being in the FF of the antenna under test (AUT). When the facility was originally commissioned, NF metrology was in its infancy [6, 7], and facilities were custom-made, both in terms of hardware and software. In the interim, commercial products, with ongoing technical support, have become available [8]. As our antenna range is a general purpose facility, it was upgraded as a NF range, given the flexibility offered by such a system, although some initial consideration was given to converting the anechoic chamber into a tapered range, similar to [9].

In this paper, the upgrade of this facility is detailed. This begins with an overview of the upgrade process, specifically the changes made to support the new components. This is followed by a description of the functions of the components, focusing on the options provided by the NF measurement types. Thereafter, a description of the measurement setup is provided, including the calibration process required prior to performing a measurement. The paper concludes

with initial results using the facility; several innovative commissioning tests, which represent new contributions in the context of this range; and an outline of ongoing and planned work to further improve the facility.

2. UPGRADE PROCESS

While the manufacture of antenna measurement systems is a specialised field in general, this is particularly true for NF ranges. Therefore, Nearfield Systems, Inc. (NSI), a US based company, was contracted to drive the upgrade of Stellenbosch University's facility [10]. This company has been providing hardware, software and customer support for antenna metrology for over a quarter of a century. Of particular interest is the integration of NSI's components with that of Keysight Technologies' range of VNAs, as our research group had extensive experience using their VNAs.

Both planar motions and spherical motions are required to provide support for both high gain and low gain antennas, as each motion type is appropriate for a different gain type, with this upgrade including both in an integrated system. The 700S-30 was identified as an appropriate model for the spherical motions, in supporting antennas up to 0.5 m in diameter and up to 18 kg in mass. This spherical near-field (SNF) scanner supports medium and low gain antennas in sampling the full sphere around the AUT and the existing PNF scanner supports high gain antennas in sampling a finite sector of the forward hemisphere of the AUT.

Before the upgrade was initiated, the state of components was catalogued, to determine which components to replace and which to retain. The absorber material, PNF scanner and Z Track were in good condition, despite providing over a quarter century of service. For reasons outlined above, it is useful to have *both* PNF and SNF scanners available, and it proved cost effective to integrate these into one system, making use of the Z Track to shift the SNF scanner to allow for both measurement types – and potentially CNF – using the same equipment. It should be noted that this facility can only support one measurement type at any given time.

Although still functional, the cylindrical axis rotator was rendered redundant by the procurement of the SNF scanner. Similarly, the new control equipment rendered the motors and the encoders of the PNF scanner redundant. While the SNF scanner is designed to be mounted on the floor, a wheeled base was designed at Stellenbosch University to manually shift it along the Z Track to the desired separation from the probe. This base positions the AUT at the anechoic chamber's mean height, maximising the scan area and positioning the AUT in the quiet zone.

3. SYSTEM COMPONENTS

Stellenbosch University's antenna range comprises the control equipment, primarily housed in the control room; the motion stages, housed in the anechoic chamber; and the control and RF cabling connecting the various components in and between these two rooms. The control equipment comprises the motion stage controllers; the workstation running the data processing software; and the VNA, which acts as both the RF source and receiver. The motion stages comprises the various motors, motor drivers and support structures for the planar and spherical scanners. All these components, and the probes, are described in this section.

3.1 Control Room

The control room forms part of a larger workspace, which includes the laboratory manager's office and the storage area for the antenna range's interchangeable components. This room shares a dry wall with the anechoic chamber, which contains the interface for the control and RF cabling to pass between these two rooms and the door for personnel to gain access to the anechoic chamber. The control room has a grounded workbench, on which the majority of the control and measurement equipment are housed.

The user utilises a desktop workstation in order to perform measurements. The data processing software is installed on this workstation, which allows the user to interact virtually with the hardware, with the complicated process of controlling and synchronising the motor movements with the measurement sampling hidden from the user. However, the user must understand the limits of the antenna range, as it is possible to override the hardware and software safeguards during the calibration process.

In taking the measurements, the VNA is a core component. The PNA-X 5242A was identified as an appropriate model due to its performance, integration with NSI components, and our familiarity with its predecessors. It is also used for numerous other measurement types [11]. While the new VNA covers the same frequency range as the previous one, the speed at which it switches between frequencies is much faster. This allows the two scanners to move continually during measurements, greatly speeding up the process.

The control and synchronisation of the motor movements with the measurement sampling is performed by the primary controller. This device converts requests made by the user in the data processing software into commands for both the VNA and the motors. It also records the motor movements and the measured samples. These records are synchronised and stored on the desktop workstation. Once the measurement set has completed, the user interacts with the data processing software to generate the desired results.

Additionally, the primary controller directly controls the SNF scanner's motors and indirectly controls the PNF scanner's motors through the secondary controller. Whilst part of the control equipment, the secondary controller is housed inside the anechoic chamber behind the X Track to reduce the length of, and therefore loss in, the power cabling. Due to the mass of the Y Tower, motor drivers are utilised to provide the x stage and y stage with sufficient power. None of the other stages require motor drivers.

The control room is equipped with an uninterruptible power supply in the event of a power outage, allowing the components to be shut down gracefully. No mechanical

damage is expected, as the lead screws of the PNF scanner hold the Y Tower and the probe in place. A minimum measurement set is lost, as the data is stored on the desktop workstation after each scan. However, the motor positions require recalibration after a power outage, with the option of resampling a portion of the scan area for verification.

3.2 Anechoic Chamber

The anechoic chamber is a rectangular room of dimension 9.1 m (L) × 5.5 m (W) × 3.6 m (H). Several modifications were required when the chamber was constructed in the 1980s, as this room was originally an acoustic chamber. To shield the room from external signals, the interior surfaces were covered with aluminium sheeting, with the joints soldered together to create a Faraday cage. As is usual with an anechoic chamber, the interior surfaces of the flooring, walls and ceiling were covered with absorber pyramids.

The back wall is covered with commercially supplied absorber pyramids of 18 inch (450 mm) in height, with the other surfaces covered with absorber pyramids of 12 inch (300 mm) in height. The absorption of these pyramids at a particular frequency is better the taller the pyramid, with 18 inch pyramids specified down to 500 MHz and 12 inch pyramids down to 1 GHz. There is a walkway made from absorber material running parallel to the Z Track, allowing personnel to traverse the length of the anechoic chamber.

Although the walkway is made out of absorber material, it has different properties to the pyramids. Using the ability of the SNF scanner to rotate both rotation axes beyond 360°, it is possible to perform SNF measurements over a complete sphere with or without orientating the AUT in the direction of the walkway. This will be used later in this paper to quantify the performance variance between the pyramids and the walkway.

To screen the AUT from the reflective surfaces of the PNF scanner, two wooden panels are mounted onto the Y Tower, with the surface of these panels facing the AUT covered with absorber pyramids. Similarly, to screen the probe from the reflective surfaces of the SNF scanner, the L Bracket is covered with absorber pyramids. In both cases, these absorber pyramids are 8 inch (200 mm) in height, and are specified down to 1 GHz. However, the reflective surfaces of the SNF base remain untreated.

The sections of the floor and roof that the Y Tower passes along during PNF measurements are free of absorber pyramids, to avoid fouling the Y Tower. The lead screw for the X Track runs above the floor level, making it difficult to screen this section of the floor with absorber pyramids. As there is no hardware at ceiling level, the aluminium sheeting here was covered with non-reflective material. Over this, velcro strips were installed, so that absorber pyramids could be attached during SNF measurements.

A section of the floor behind the X Track has been cleared of absorber material to house the secondary controller. The opening is larger than the volume of this controller to allow the control cabling to be connected to the back panel and to give personnel access to the switches on the front panel. Additionally, space was made to not block its cooling vent on the side panel. While non-ideal from a RF interference point of view, this controller is housed near the PNF scanner to provide its motors with sufficient power.

3.3 Planar Scanner

The PNF scanner comprises the X Track embedded in the floor of the anechoic chamber, the Y Tower mounted on the X Track, and the polarisation stage mounted on the Y Tower. To move the probe along the x axis, the *x* stage translates the Y Tower along the X Track. To move the probe along the y axis, the *y* stage translates the pol stage along the Y Tower. To rotate the probe around the polarisation axis, the pol stage rotates the probe. These three stages are controlled by the secondary controller.

The existing X Track and Y Tower were retained, with the two motion stages replaced and the pol stage redesigned. The *x* and *y* stages comprise motors and drivers that move the probe over a 2.6 m (x axis) × 2.0 m (y axis) scan area, with minimum step sizes of 0.025 mm (x axis) and 0.0125 mm (y axis) at speeds of 0.1 m/s (x axis) and 0.05 m/s (y axis). The pol stage comprises a motor and rotary joint, that rotates the probe between polarisations, with a minimum step size of 0.0125° at a speed of 20°/s.

The gap between the absorber panels on the Y Tower can be adjusted to accommodate probes of varying dimension. However, the wider the gap, the greater the surface area of the reflective surfaces of the Y Tower that is seen by the AUT. Therefore, to maximise the probe support and to maximise the Y Tower absorber coverage, the pol stage is housed behind the absorber panels, with only cabling and a support beam passing between the absorber panels. This does limit the probe mass supported by the Y Tower.

There are three different safety mechanisms in place to prevent the *x* stage and the *y* stage from derailing the PNF scanner. Soft limits restrict the movements of the PNF scanner to within the bounds set by limit switches mounted on the X Track and the Y Tower. Hard limits cut the power to the motors in the event that these switches are passed, with hard stops mounted on the ends of the X Track and the Y Tower. The pol stage is fitted with a rotary joint to prevent the cabling from wrapping around the Y Tower.

The PNF and SNF scanners are depicted in Figure 1.

3.4 Spherical Scanner

The SNF scanner comprises the 700S-30 scanner mounted on the SNF scanner base, which is mounted on the Z Track, which is embedded in the floor of the anechoic chamber. To move the AUT along the z axis, the SNF scanner is manually translated along the Z Track. To rotate the AUT around the θ axis, the θ stage rotates only the L Bracket of the SNF scanner. To rotate the AUT around the ϕ axis, the

Figure 1: Anechoic Chamber

Figure 2: Spherical Near-Field Scanner

ϕ stage rotates the AUT. As the Z Track is not absolutely flat, the SNF scanner is levelled after each translation.

The existing Z Track was retained, with the SNF base manufactured internally at our university, with the other components forming part of the upgrade. The θ stage and the ϕ stage comprise motors and rotary joints that rotate the AUT over a 360° (θ axis) $\times$ 360° (ϕ axis) spherical scan area, with step sizes of 0.0125° (both) at speeds of 20°/s (ϕ axis) and 7.3°/s (θ axis). There are three measurement setups: 180° (θ axis) $\times$ 360° (ϕ axis), 360° (θ axis) $\times$ 180° (ϕ axis) and the redundant 360° (θ axis) $\times$ 360° (ϕ axis).

The AUT is offset from the mounting interface of the SNF scanner. This is done to reduce SNF measurement times by reducing the offset between the AUT and the θ axis, with this axis running through the centre of the SNF base. Also, this protects the absorber pyramids by offsetting the volume in which the AUT and RF cabling rotate during SNF measurements from the volume occupied by the absorber pyramids on the SNF scanner. However, this does limit the AUT mass supported by the SNF scanner.

Unlike for the PNF scanner, no rotation of the ϕ stage nor the θ stage could potentially derail the SNF scanner. Soft limits on the θ stage are used to align the AUT as part of the calibration process and to prevent the cabling from wrapping around the SNF scanner. The θ stage has no hard limits, as the 360° rotations that form part of SNF measurements prohibit their use. The ϕ stage has no limits, with alignment determined with a level and a rotary joint preventing the cabling from wrapping around the scanner.

The SNF scanner is depicted in Figure 2.

3.5 Probes

The operational properties of the four currently available probes are listed in Table 1. While the rectangular probes are suitable for both measurement types, the horn probe (RGP-10) is restricted to SNF measurements, due to the nulls in the forward hemisphere of the radiation pattern of this probe, which would cause errors in the PNF probe correction algorithm. If required, users can provide their own probes, with compatible mounting brackets, and implement their own probe correction on the NF data.

Table 1: Probe Operational Properties

Probe	Frequency Range	Measurement Type
RGP-10	0.7–5.0 GHz	SNF
WR137	5.85–8.2 GHz	PNF, SNF
WR90	8.2–12.4 GHz	PNF, SNF
WR62	12.4–18 GHz	PNF, SNF

As the antenna range supports PNF and SNF measurements, with the potential to include CNF measurements, it is desirable to have probes suitable for both measurement types over as wide a frequency range as possible. However, the size and weight of low frequency rectangular probes would strain the load capacity of the scanners. Therefore, a horn probe is used, which is smaller and lighter than the comparable rectangular probes and which has a wider operational band than the comparable rectangular probes.

Each probe has a kit comprising absorber collar, mounting bracket and waveguide to coaxial transition, as depicted in Figure 3. The absorber collar hides the reflective surfaces of the RF cabling and mounting interface from the AUT. The mounting bracket allows the probes to be mounted on both scanners. For the rectangular probes, the waveguide to coaxial transition is positioned behind the absorber collar, while for the horn probe it is in front of the absorber collar, but hidden from the AUT by the horn's flanges.

3.6 Anechoic Chamber Layout

The anechoic chamber layout is depicted in Figure 4. The PNF scanner is the Y Tower mounted on the X Track and

(a) Horn Probe (b) Rectangular Probe

Figure 3: Probe Kits

the SNF scanner is the L Bracket mounted on the Z Track. The probe mounting interface is in front of the absorber panels, limiting the maximum AUT to probe separation to 6.0 m, and the AUT mounting interface is on the L Bracket. The Z Track is offset from the mean width to accommodate the walkway. While the Y Tower can transverse the full X Track, its nominal position is aligned with the Z Track. If the dimensions or mass of the AUT exceed the limits of the SNF scanner, the SNF scanner could be moved out of the way, with a suitable stand manufactured for the AUT. Only PNF measurements could be made in this case.

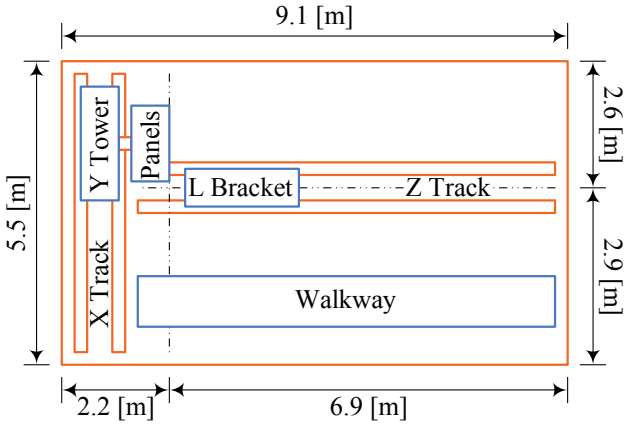

Figure 4: Anechoic Chamber Layout

The coordinate system of the anechoic chamber is depicted in Figure 5. Positive θ rotation is clockwise as seen from above the AUT and positive ϕ rotation is counter clockwise as seen from behind the AUT. As seen from in front of the probe, positive x translation is leftward, positive y translation is upward, positive z translation is backward and positive polarisation rotation is clockwise. During calibration, the x stage, y stage and θ stage move in their negative directions to determine their nominal positions. The definition of θ and ϕ rotations are opposite to those normally used; for our facility, the AUT moves during SNF measurements, whilst the probe remains stationary. (Conventionally in antenna theory, the AUT is stationary, at the centre of the coordinate system, and the fields around it are probed as a function of θ and ϕ.)

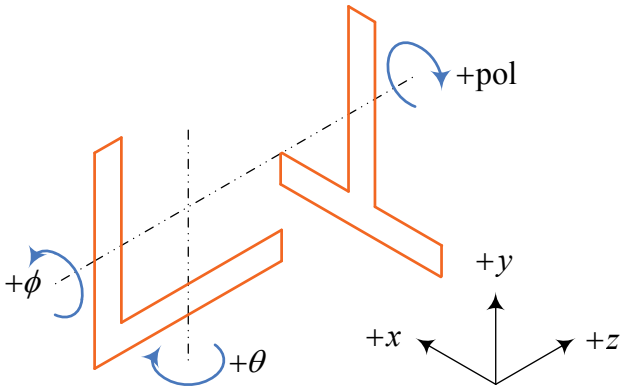

Figure 5: Anechoic Chamber Coordinate System

3.7 *Antenna Range Layout*

The control interface is depicted in Figure 6. The primary controller converts the user's interactions with the desktop workstation into synchronised movements of the SNF scanner (directly) and PNF scanner (via the secondary controller) with measurement sampling by the VNA. The x stage and y stage require drivers to move the Y Tower.

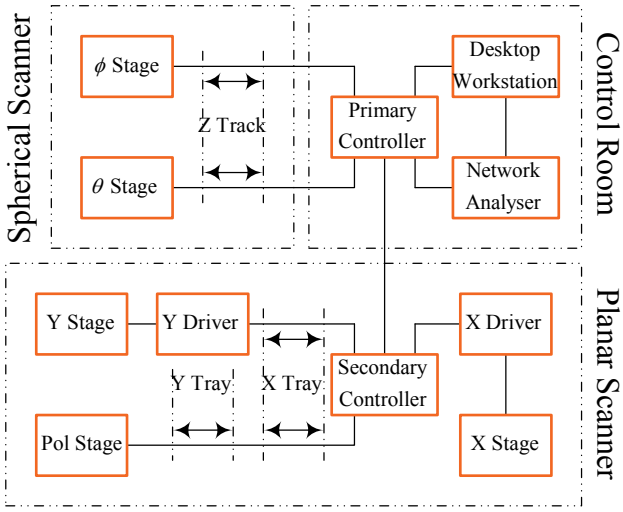

Figure 6: Control Interface

The RF interface is depicted in Figure 7. The VNA compares the signal transmitted by the AUT with the signal detected by the probe and amplified by the amplifier. The θ stage, ϕ stage and pol stage are fitted with rotary joints.

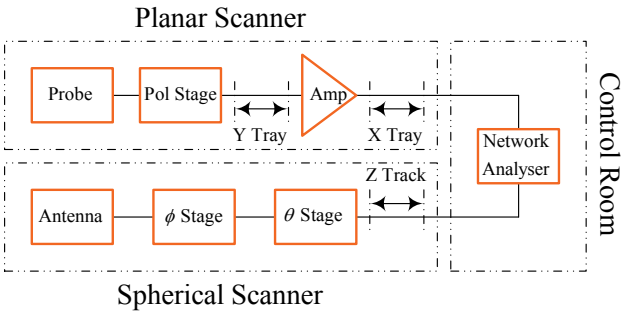

Figure 7: RF Interface

The power interface is depicted in Figure 8. The secondary controller and drivers are housed in the anechoic chamber to provide the PNF scanner with sufficient power.

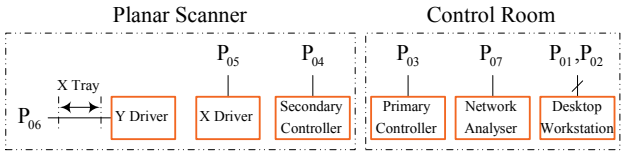

Figure 8: Power Interface

4. MEASUREMENT PROCESS

Making high quality measurements at an antenna range requires attention to NF and FF metrology theory in terms of understanding the motions of the scanners, setting up the measurement, designing a suitable mounting interface for the AUT, calibrating the antenna range and correcting for probe effects. All of these are described in detail in this section. While the mathematics surrounding NF to FF transformations are beyond the scope of this paper, a brief introduction into the theoretical background is given.

As FF patterns are the end result of most measurements, it would appear logical to place the probe in the FF — and indeed, this is a standard requirement in a far-field range. Generally, the FF is established at $2D^2/\lambda$ from the antenna, where D is the largest dimension of the antenna and λ is the wavelength [12]. This distance might be inadequate for high-precision measurements and could become excessive for electrically large antennas or low frequency measurements. In such cases, the probe is placed in the radiating NF, with NF to FF transformation used to compute the FF data [8].

During PNF measurements, the position and orientation of the AUT remains constant throughout, while the probe is twice moved over a planar surface in front of the AUT, with the orientation of the probe rotated 90° between scans to measure orthogonal polarisations. As only the forward hemisphere of the AUT is sampled, PNF measurements are best suited for high gain antennas. As the AUT remains at rest throughout the measurement, PNF measurements are best suited for antennas that are large, heavy and/or flimsy.

By contrast, during SNF measurements, the AUT is twice moved over a spherical surface in front of the probe, while the position and orientation of the probe remains constant for each scan, with the orientation of the probe rotated by 90° between scans for polarisation purposes. As the sphere around the AUT is sampled during SNF measurements, these measurements are best suited for low gain antennas. As the AUT is in motion throughout, SNF measurements are best suited for small, lightweight and sturdy antennas.

During PNF measurements, the orientation between the AUT and the probe varies throughout, with the probe sampling the AUT fields at angles off the probe's boresight. As such, the probe's radiation pattern should have no nulls in its forward hemisphere. While the main beam of a horn probe would be too narrow, a rectangular probe would have the desired radiation pattern. However, the operational band of a rectangular probe is limited, requiring multiple probes to span the full band at our facility.

By contrast, during SNF measurements, the orientation of the probe remains fixed on the AUT throughout, with the probe sampling the AUT fields on the probe's boresight. This allows a probe with a narrower main beam to be used, as the sector of the probe's radiation pattern that must be null-free is reduced. While rectangular and horn probes can be used, horn probes have the advantages of operating over a wider frequency range than rectangular probes and are lighter than rectangular probes at low frequencies.

4.1 Planar Near-Field Measurements

The probe motion during PNF measurements is depicted in Figure 9. The probe is translated the full y axis in one direction, then translated the sampling distance, Δx, in the x axis, before being translated the full y axis in the opposite direction. Once the full x axis is traversed, the probe is rotated and then it traces its path in the reverse direction. While both x over y and y over x are possible, y over x is the default as y translation is faster than x translation.

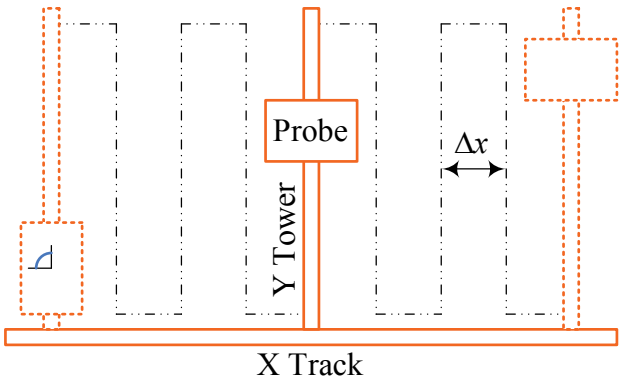

Figure 9: Planar Near-Field Measurement Motions

The PNF measurement setup is depicted in Figure 10. The probe travel length, L, is determined by the relationship

$$L \approx D + 2Z\tan\alpha \qquad (1)$$

where D is the AUT diameter, Z is the AUT-to-probe separation, and α is the scan angle. As the probe must be in the radiating NF, Z is usually set to 3λ. Since the probe must detect as much of the energy in the NF as possible, α is chosen large enough to encompass all the significant NF energy; typically, 40 dB below peak is used as the criterion.

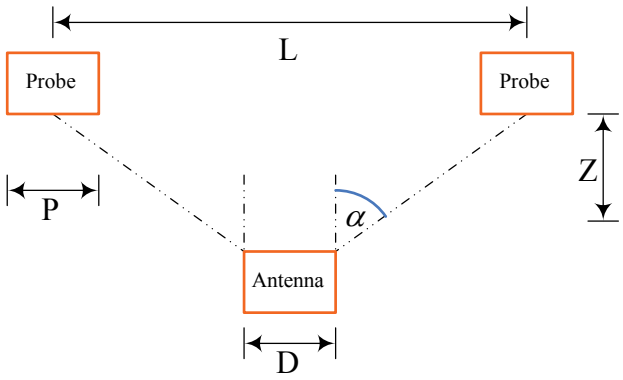

Figure 10: Planar Near-Field Measurement Setup

The SNF scanner can be shifted nearer the PNF scanner and/or a bracket can be mounted on the SNF scanner's mounting interface to reduce the AUT to probe separation. This would reduce the probe travel length for a given scan angle, reducing the measurement time. However, the probe must remain in the radiating NF. Similarly, the bracket cannot overload the SNF scanner's bending moment nor misalign the AUT from the centre of rotation of the ϕ stage.

4.2 *Spherical Near-Field Measurements*

The probe and AUT motions during SNF measurements are depicted in Figure 11. The AUT is rotated the full θ axis in one orientation, then rotated the sampling distance in the ϕ axis, before being rotated the full θ axis in the opposite direction. Once the full ϕ axis is rotated, the probe is rotated, before the AUT traces its path in the reverse direction. While both θ over ϕ and ϕ over θ are possible, ϕ over θ is the default as ϕ rotation is faster than θ rotation.

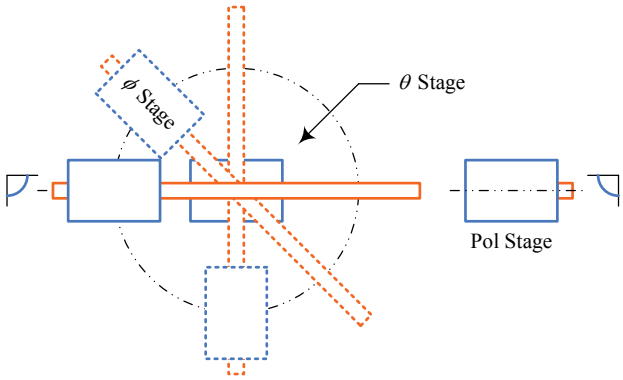

Figure 11: Spherical Near-Field Measurements Motions

The SNF measurement setup is depicted in Figure 12. The scan centre is the intersection of the θ and ϕ axes, with the probe aligned with the ϕ axis. MRS is the minimal radius sphere, which is the spherical volume around the scan centre that the AUT fills during SNF measurements. PSR is the probe scan radius, which is the distance between the probe and the scan centre. The smaller the minimal radius sphere, the shorter the measurement time. The shorter the probe scan radius, the lower the free space losses.

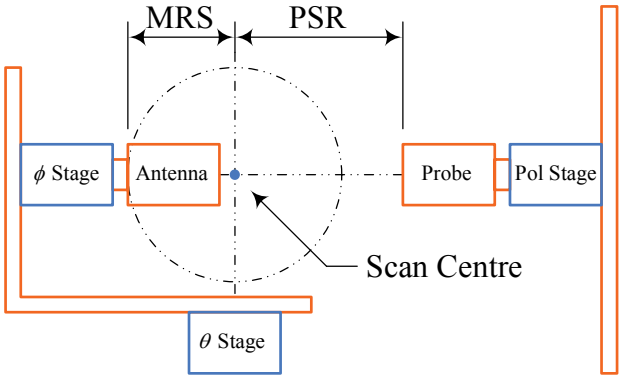

Figure 12: Spherical Near-Field Measurement Setup

A bracket can be mounted on the SNF scanner's mounting interface to place the AUT closer to the θ stage's centre of rotation. This would reduce the volume that the AUT fills, reducing the measurement time. However, this bracket must not overload the SNF scanner's bending moment nor misalign the AUT from the ϕ stage's centre of rotation. The SNF scanner can be shifted nearer the PNF scanner. However, the probe must remain in the radiating NF.

4.3 *Calibration Process*

Before the calibration process begins, the components in the antenna range are switched on, with the order equal to the inverse of the hierarchy of the control equipment: motor drivers; secondary controller; VNA; desktop workstation; primary controller; and data processing software. It is advisable to switch the VNA, the power amplifier and the cooling system on an hour before the measurement sampling starts to allow the temperature in the anechoic chamber and these components to stabilise.

Preceding calibration, it must be determined whether the AUT can indeed be measured at the range. This requires that the AUT operates at a frequency range compatible with the probes, that the AUT has an interface that is compatible with the SNF scanner, and that the AUT does not overload the SNF scanner's bending moment. While the choice between SNF and PNF measurements is usually determined by the antenna's directivity, the former might be excluded if the AUT is too heavy or fragile to be rotated.

Given this, the first step in the calibration process is to mount the AUT and the probe onto the scanners. This is required to determine the positioning of the SNF scanner

along the Z Track, as well as any resizing of the standoffs of the AUT's mounting bracket. To minimise measurement time, it is preferable to position the AUT as close as possible to the probe during PNF measurements, while it is preferable to position the AUT as close as possible to the centre of rotation of the θ stage during SNF measurements.

A mounting bracket was designed for the AUT, as depicted in Figure 13. The back interface is compatible with the mounting interfaces of the PNF and SNF scanners. While the front interface has several mounting holes, users can interchange it for one that is compatible with their AUT. The absorber collar, comprising 6 inch absorber pyramids, hides the reflective surfaces around the ϕ stage from the probe, with the components in front of the collar made of perspex. The gap in the collar is to allow cabling through.

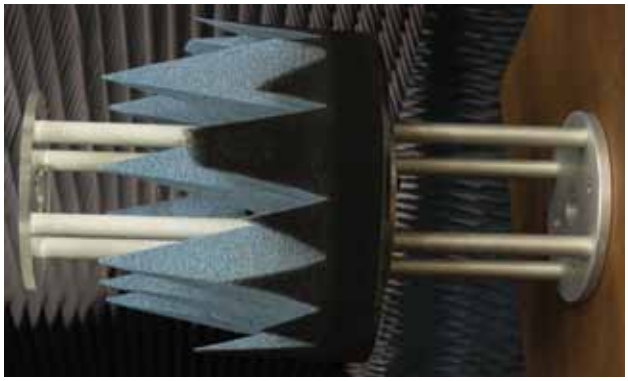

Figure 13: AUT Bracket

If the Z Track has been repositioned, the SNF scanner needs to be realigned, due to the non-ideal alignment of the Z Track with the floor of the anechoic chamber. When repositioning the Z Track, one should ensure that the RF cabling connected to the SNF scanner is the optimal length to minimise RF cable losses. Once the probe and the AUT have been mounted, they are aligned with each other for polarisation purposes. However, the data processing software can correct for misalignment during processing.

The polarisation setup for devices, both probes and AUTs, is depicted in Figure 14. The principal polarisation is at 0°, and this is when the connector is on the left of the device. The cross polarisation is at 90°, and this is when the connector is on top of the device. The definition for polarisation is when the user is in front of the device and looking at the device. Polarisation alignment is achieved by placing a spirit level on top of the probe for the pol stage and similarly on top of the AUT for the ϕ stage.

As no method to determine the positions of the x stage, y stage and θ stage has been implemented, their positions are calibrated each time their motors are switched on. Their motors are indexed by moving them in the direction of their safeguards, which are located at exact positions. Once these safeguards have been reached, the motors are able to reposition themselves relative to these positions. However,

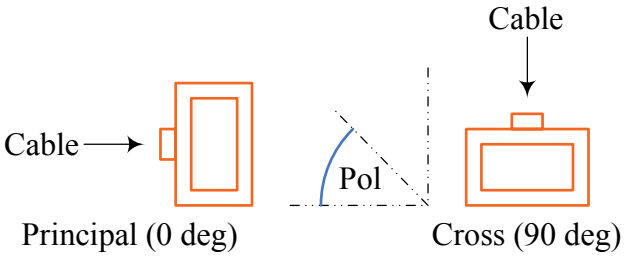

Figure 14: Polarisation Setup

a method to independently monitor whether the motors are moving as expected has not been implemented.

Once the calibration process has been completed, it is advisable to perform a few sanity checks. The power levels detected by the probe should drop when the probe's polarisation is rotated. For PNF measurements, one should ensure that the PNF scanner's motions will not crash the probe into the walkway. For SNF measurements, one should ensure that the cabling will not wrap around the SNF scanner. With the data processing software set on stability check, one should ensure that the RF cabling has been properly torqued.

Probe correction requires data about the probe in one of three forms: analytical model, simulation model or measurement data. Analytical models are suitable for probes with predictable radiation patterns and that have low on-axis cross polarisation levels, such as rectangular probes [13]. For complex probe types, such as horn probes, where the radiation pattern cannot be accurately predicted, simulated or measured data is required, with measurement data preferred due to manufacturing tolerances [14].

In the antenna range, probe correction forms part of the NF to FF transformation algorithm, with the option of selecting between an analytical model, only available for the three rectangular probes, or importing third party data, with measurement data available for the horn probe. With this option, users are free to import third party data for the rectangular probes or for their own probe, if needed. Otherwise, the raw NF data can be exported, allowing users to apply their own NF to FF transformations.

5. COMMISSIONING TESTS AND RESULTS

The commissioning of this facility is an ongoing process, as different measurements uncover new aspects of the facility. In this section, initial test of the facility and initial measurements using the facility are presented.

5.1 Stability Check

The stability check option has uncovered a stability problem with the RF cabling at the rear of the PNF scanner. With the system at rest, the RF cabling in the region of the amplifier is wiggled by hand, with the resulting phase change depicted in Figure 15. The phase does not return to the original value after the wriggle and the

magnitude of change that the phase undergoes during the wriggle is excessive. Therefore, replacement cables are being investigated. The SNF scanner has no such similar problem.

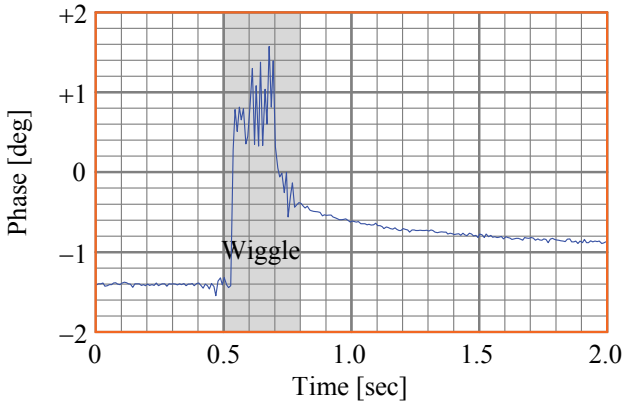

Figure 15: Stability Check

Before each measurement, a sample is taken at a point in the high energy zone of the AUT, and after each measurement, another sample is taken at the same point. The difference between these two measurements is an indication of the amplitude and phase drift during the measurement. Irrespective of frequency, our system has a ± 0.1 dB and $\pm 1^\circ$ drift for an hour long measurement. As an example, the stability check option is used to show that the rotation of the pol stage from 0° to 90° and back to 0° has a minimal effect on the amplitude and a marginal effect of the phase of the measurement, as depicted in Figure 16.

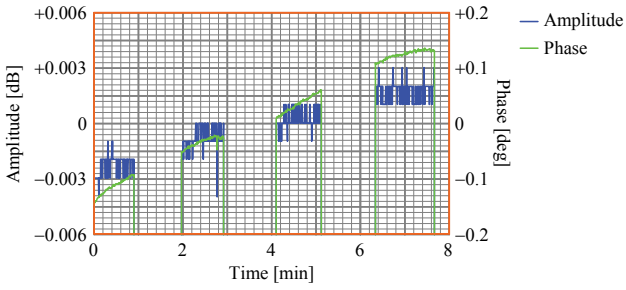

Figure 16: Drift Check

5.2 *Alignment Check*

As part of the installation process, a five point laser was used to align the axes of the five automated stages and to align the mounting interfaces of the pol and ϕ stages. During the calibration process, the distances from this alignment point to the negative limit switches along the X Track, along the Y Tower and in the θ rotation stage are used to realign the x, y and θ stages, while the pol and ϕ stages are aligned using a spirit level. While this mechanical alignment is accurate, machining tolerances for the mounting brackets could introduce deviations.

During initial testing, deviations of the order of ± 1 cm (x and y axes), $\pm 1^\circ$ (θ axis) and ± 1 mm (pol and ϕ mounting interface) have been recorded. These deviations have a greater effect at higher frequencies and on the phase, potentially leading to artefacts in the transformed FF patterns. As an example, two SNF measurements are taken, with a deliberate misalignment of the y axis introduced before the second measurement, resulting in the sharp contrast between the FF transformations depicted in Figure 17.

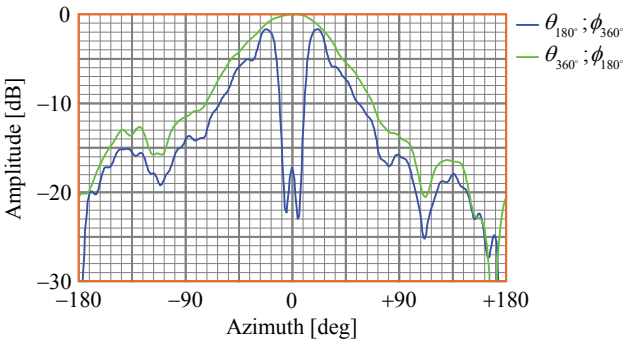

Figure 17: Can Antenna ($\phi = 0$ deg)

Electrical alignment is used to correct for any mechanical deviations. Two cuts along the same plane are measured, with the polarisation of the AUT rotated by 180° between cuts, with any deviation between the cuts attributed to a mechanical misalignment. A discrepancy in the amplitude between the two cuts indicates the offset from the axis, as depicted in Figure 18, while a discrepancy in the phase indicates the offset from the mounting interface.

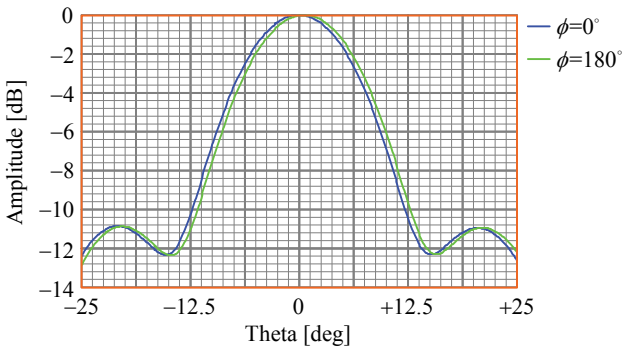

Figure 18: Alignment Check

5.3 *Determining Chamber Reflection Levels*

The effect of exposed reflective surfaces in the chamber has been investigated using SNF measurements of a standard gain horn with the WR137 probe, as depicted in Figure 19. The probe is shielded from reflections off the Y Tower by its collar, as indicated by the marginal effect on the pattern when the gap between the absorber panels is narrowed. Similarly, the probe is shielded from reflections

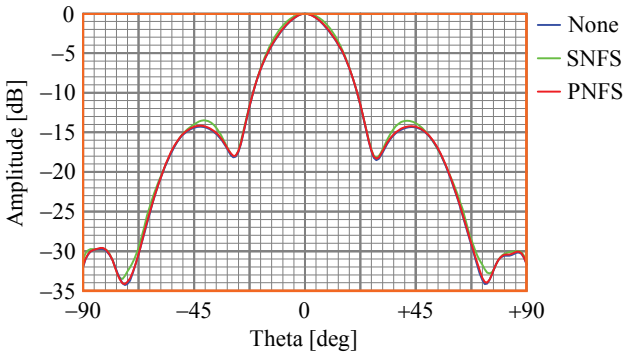

Figure 19: Reflection Check ($\phi = 0$ deg)

off the L Bracket by the AUT's collar, as indicated by the noticeable effect on the pattern when this collar is added.

The absorber pyramids that the chamber is covered with are specified down to 1 GHz; however it is desirable to extend use of the chamber down to at least 0.75 GHz. Therefore, the method outlined in [8, §8.10] has been used to quantify the level of reflection from the chamber at low frequencies. The underlining principal is that if the distance between the AUT and the source of reflection is changed by $\lambda/4$, the comparison between the two measurements can be used to separate the desired signal from the reflected signal.

As an example, measurements have been taken to determine the chamber reflection at 0.75 GHz, which is below the lower limit specified for the absorber pyramids, as depicted in Figure 20. The probe and the AUT are separated by a fixed distance for the first measurement, with both translated by $\lambda/4$ for the second. The effect of reflections off the probe is equivalent in both measurements, as the separation between the AUT and probe remains constant. The result indicates a chamber reflection level of below -30 dB.

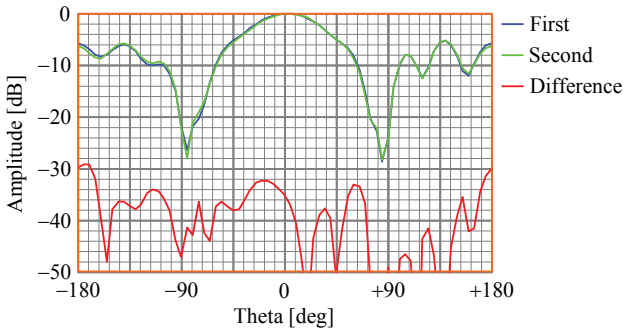

Figure 20: Chamber Reflection

A feature of our indoor antenna range is the ability to take redundant SNF measurements. The AUT can be rotated 360° around both the θ axis and the ϕ axis, resulting in the radiated fields over the full sphere being sampled twice, but with different configurations of the AUT with respect to the chamber. For instance, a full NF measurement can be performed with the AUT rotated from 0° to +180° around the θ axis, which directs the AUT towards one side of the chamber, and a full redundant NF measurement can be performed with the AUT rotated from 0° to −180° around the θ axis, which directs the AUT towards the other side of the chamber, as depicted in Figure 21. For both measurements, the AUT is rotated 360° around the ϕ axis.

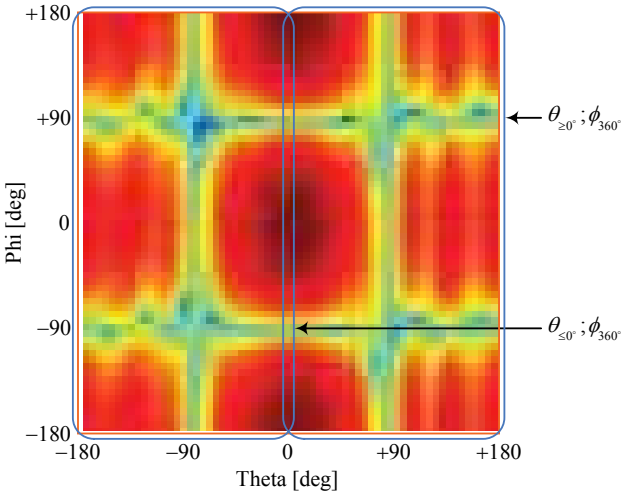

Figure 21: Redundant Near-Field Measurement

Theoretically, these two SNF measurements should transform to equivalent FF patterns. However, the poor absorptive properties of the absorber material used in our chamber at lower frequencies, and especially below the specified 1 GHz limit, result in radiated fields being reflected off the walls of chamber back towards the probe. The offset position of the SNF scanner to make room for the walkway results in a disparity in the signal path on opposite sides of the AUT, which is more pronounced at lower frequencies. The combination of these two phenomena result in a disparity in the radiated fields detected by the probe when the AUT is directed to the opposite sides of the chamber at 0.75 GHz, as depicted in Figure 21.

This disparity between the NF measurements results in a variance between the computed FF patterns. This variance is more pronounced at lower frequencies than at high frequencies, as depicted in Figure 22. For example, the RMS value between the two principal Azimuth cuts is -25.3 dB at 0.75 GHz, while at 3 GHz it is -32.3 dB. To quantify the disparity between the two sets of redundant SNF measurements, the RMS difference between the two sets of computed FF patterns is calculated over the whole sphere for a range of frequencies, as depicted in Figure 23. As expected, this disparity is larger at lower frequencies, especially below the specified 1 GHz limit, and it is not improved by replacing the walkway with pyramids.

Using these calculated RMS values, the measurement uncertainty in the computed FF patterns at 0.75 GHz is depicted in Figure 24. Depending on the measurement configuration, the actual FF pattern of the AUT would be

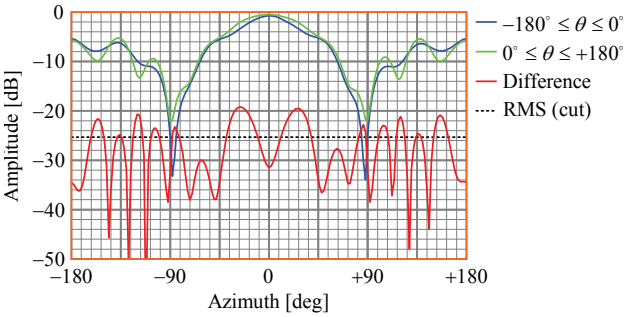

(a) 0.75 GHz

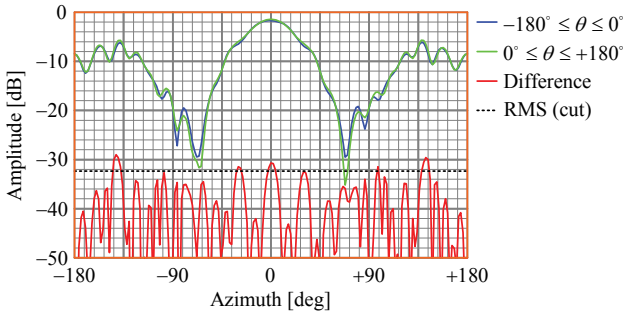

(b) 3.0 GHz

Figure 22: Redundant Spherical Measurements

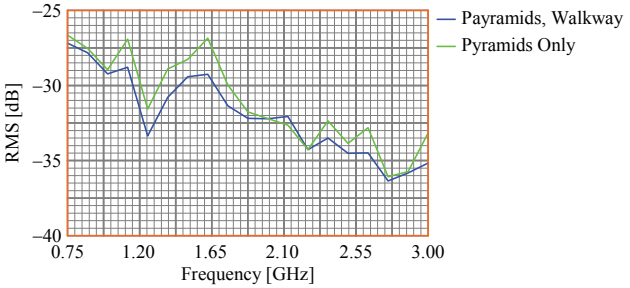

Figure 23: RMS Disparity between Computed Far-Field Patterns

within the RMS envelop around the computed FF pattern. (The specific AUT in this case is a commercial biconal antenna, with operating band 500 MHz — 3 GHz). Such a plot could be used to determine the certainty with which the measured AUT meets the design requirements.

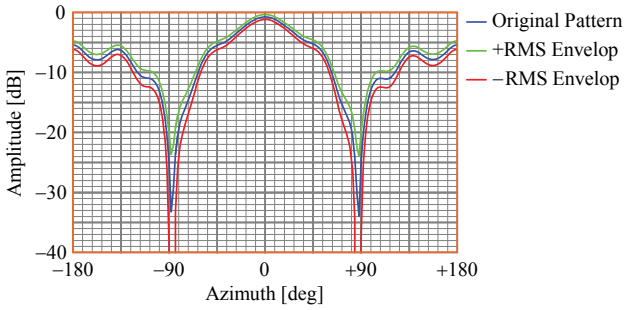

Figure 24: Far-Field Cut with RMS Envelop

5.4 Measured Results for a Patch Antenna

To demonstrate the functionality of the antenna range, the FF patterns of a circular polarised patch antenna were determined. This antenna operates over the 2.4 GHz to 2.5 GHz frequency range and has dimensions of 32 cm (L) × 8 cm (W). As the FF starts at 1.75 m, the FF patterns can be determined by transforming NF measurements into FF data or by taking FF measurements. Both options were chosen, to compare the results of these two types.

For the measurements, the horn probe was attached to the PNF scanner, and the patch antenna was attached to the SNF scanner. The only change to the measurement setup between measurements, was to shift the SNF scanner along the Z Track, moving the probe from inside the radiating NF to the FF. To validate the comparison, the measurements were performed to generate equivalent FF data sets, that of a θ span of 261° and a ϕ span of 360°, at intervals of 3°.

For the FF measurement, the AUT to probe separation was 4.9 m, with a scan area of 261° (θ) × 360° (ϕ) sampled at 3° intervals. For the NF measurement, the probe scan radius was 1 m and the minimal radius sphere was 0.16 m, with a scan area of 171° (θ) × 360° (ϕ) sampled at 9° intervals. While the measurement times are equivalent, the data processing software can zero pad the NF data to improve the resolution of the projected FF data.

Both measurement types provide accurate patterns of the antenna, with the principal cuts at 2.45 GHz for the two measurement sets depicted in Figure 25. The difference between the two results is minimal, less than 2 dB on the flanks of the main lobe and less than 4 dB for the side lobes. This discrepancy is as a result of the difference in the environment between the two measurement sets; in changing the separation, the signal path was changed.

6. FUTURE WORK

The necessity to improve the absorber coverage in the anechoic chamber is under investigation. The focus is on components that are visible to the probe, as it is the probe's response to the signal transmitted by the AUT that is measured. The SNF scanner will receive attention in the form of an absorber coverage for its base and the PNF scanner will receive attention in the form of absorber coverage for the X Track for SNF measurements.

Work is in progress to expand the frequency range of the anechoic chamber. To bridge the gap between the specified ranges of the probes, a standard gain horn will be measured using the probes, to determine whether the probes can be used outside of their specified ranges. To extend the frequency range beyond 18 GHz, an additional probe would be required, along with the RF cabling and connectors required to deliver the RF signal to the VNA.

The power amplifier, housed on the Y Tower, amplifies the signal levels that are detected by the probe before they are delivered to the VNA. However, the stability of this

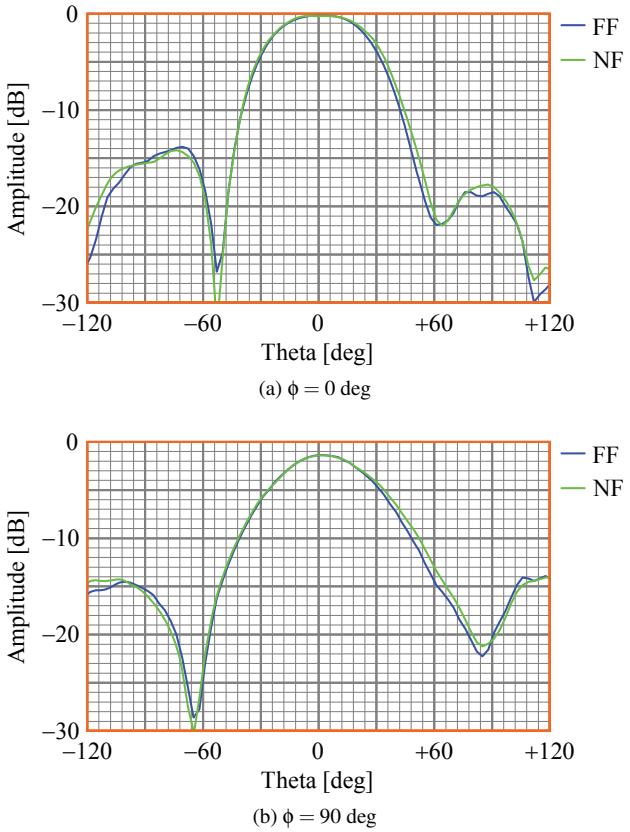

Figure 25: Principal Polarisation Cuts

amplifier is neither monitored nor controlled at present. An improved system would be to position an appropriate amplifier at the input to the VNA, making it a part of the measurement setup, with the performance of this amplifier controlled and monitored by the data processing software.

The motors are run in open-loop mode, with no feedback to control these motors' motions — nor is there an independent monitoring system for this. An improved system would be to install laser trackers to monitor the translation of the x stage and y stage. These trackers would be housed behind the absorber panels, to minimise any influence on the measurements. The data processing software would use this data to adjust the sample positions.

Although there are at present no plans to do this, it is worth stating that most, if not all, of the hardware and software required to perform CNF measurements are in place. The θ stage would provide the ϕ rotation and the y stage would provide the z translation, thereby requiring both the probe and the AUT to move throughout the measurement process. Should the specific requirements arise for a CNF scanner, it could be implemented at a very reasonable cost.

The mounting interfaces of the scanners are compatible with the probes, permitting the probes to be mounted on either scanner. However, the mounting interfaces of the scanners are not compatible with all potential AUTs. Over time, as different AUTs are measured, additional mounting brackets will be manufactured. This increase in the variety of brackets is expected to assist future measurements.

The cabling interface between the new components in the control room is different to that of the previous components. This requires a redesign of the cabling from the VNA to the interface with the anechoic chamber. There is a stability problem with the cabling at the rear of the PNF scanner, with corrective measures being pursued in the form of a pulley system and more phase-robust cabling.

7. CONCLUSION

The substantial upgrade that Stellenbosch University's indoor antenna range underwent in October 2014 has been described, as well as the initial commissioning tests. The result is the availability of FF, PNF and SNF measurements over a wide frequency range, potentially spanning from 1 GHz up to 26.5 GHz. The lower limit is set by absorber performance and the upper limit is set by the VNA. For a particular antenna, while the frequency range and directivity could suggest a particular measurement type, the weight, dimension and rigidity of the AUT could preclude, or at least depreciate, the use of certain measurement types.

This upgrade has greatly improved the ability to control and interact with the antenna range. The calibration process provides sanity checks to ensure proper configuration. The measurement process gives regular feedback, displaying intermediate measurements. The powerful processing system performs probe corrections and NF to FF transformations, as well as exporting data for analysis. The new NF capabilities have facilitated the evaluation of the chamber, such as using multiple and redundant measurements to evaluate the level of chamber reflections.

Whilst the chamber is primarily intended for Stellenbosch University staff and students, it is available to outside organisations*. The original antenna range provided almost three decades of service to Stellenbosch University's research and teaching programs in RF and microwave engineering. Given the longevity of its predecessor, it is hoped that the new facility will provide service well into the 21st century!

ACKNOWLEDGEMENTS

Funding for this major upgrade was provided by the National Research Foundation's National Equipment Program; Square Kilometre Array South Africa; the Department of Science and Technology's Research Chair Initiative; and Stellenbosch University's Strategic Fund and Engineering Faculty. All of these funding sources are acknowledged for covering the cost of approximately US$ 400 000 at the time of procurement.

*Those interested in using this facility are invited to contact the laboratory manager, Anneke Bester (annekeb@sun.ac.za) at the time of writing, who can provide mechanical drawings of the scanner interfaces to assist in the manufacture of compatible interfaces for their own devices. Raw and processed NF and FF data can be exported using a scripting tool.

This antenna range functions under the auspices of Stellenbosch University's Central Analytical Facilities Affiliated Instruments program, whose support during the procurement process is acknowledged.

The physical installation was performed by D. J. J. van Rensburg and P. N. Betjes (both of NSI), W. Croukamp (of Stellenbosch University), and the authors. Equipment, such as the SNF base as well as the brackets for the AUTs and the chamber reflection measurements, was designed and manufactured by W. Croukamp. The installation team is gratefully acknowledged, as is NSI's Project Manager, C. Smith. The photographs were taken by A. Jordaan (of Stellenbosch Centre for Photographic Services).

REFERENCES

[1] C. F. du Toit, J. Solms, K. D. Palmer, and J. H. Cloete, "Recent Progress on Cylindrical Near Field Antenna Measurements at Stellenbosch University," in *Proceedings of Joint Symposium on AP/MTT*, Pretoria, August 1988.

[2] D. E. Baker, "Evaluation and Modification of the NIAST Microwave Anechoic Chamber," in *Proceedings of Joint Symposium on AP/MTT*, Pretoria, August 1986.

[3] D. J. J. van Rensburg and C. W. I. Pistorius, "Compact Antenna Test Range at the University of Pretoria," in *Proceedings of AFRICON Conference*, Ezulwini Valley, September 1992.

[4] D. E. Baker, "User Manual for General Antenna Related Measurements at the National Antenna Test Range at Paardefontein," Gerotek Test Facilities, Paardefontein, Tech. Rep. 04/2010, August 2010.

[5] J. L. Jonas, "MeerKAT – South African Array With Composite Dishes and Wide Band Single Pixel Feeds," *Proceedings of the IEEE*, vol. 97, no. 8, pp. 1522–1530, August 2009.

[6] J. E. Hansen, *Spherical Near Field Antenna Measurements*. London: IET, 1988.

[7] D. Slater, *Near Field Antenna Measurements*. Boston, MA: Artech House, 1991.

[8] C. Parini, S. Gregson, J. McCormick, and D. J. J. van Rensburg, *Theory and Practice of Modern Antenna Range Measurements*. London: IET, 2015.

[9] D. E. Baker and R. Booysen, "High Performance Tapered Anechoic Chamber for 0.5 to 40 GHz," in *Abstracts of the SA IEEE Joint AP/MTT/EMC Conference*, Stellenbosch, April 2011.

[10] Nearfield System, Inc. Torrance. [Online]. Available: http://nearfield.com

[11] "Keysight 2-Port and 4-Port PNA-X Network Analyzer: Data Sheet and Technical Specifications," Keysight Technologies, Santa Rosa, Tech. Rep. N5242-90007, November 2014.

[12] C. A. Balanis, *Antenna Theory: Analysis and Design*, 3rd ed. Hoboken, NJ: Wiley, 2005.

[13] A. D. Yaghjian, "Approximate Formulas for the Far Field and Gain of Open Ended Rectangular Waveguide," *IEEE Transactions on Antennas and Propagation*, vol. 32, no. 4, pp. 378–384, April 1984.

[14] P. Pelland and A. Newell, "Combining Pattern, Polarisation and Channel Balance Correction Routines to Improve the Performance of Broad Band, Dual Polarised Probes," in *Proceedings of AMTA Meeting and Symposium*, Tucson, October 2014.

30-SECOND AND ONE-MINUTE RAINFALL RATE MODELLING AND CONVERSION FOR MILLIMETRIC WAVE PROPAGATION IN SOUTH AFRICA

Mary N. Ahuna[1], Thomas J. Afullo[2] and Akintunde A. Alonge[3]

Discipline of Electrical, Electronic and Computer Engineering, University of KwaZulu-Natal, Durban 4041, South Africa
[1]215000279@stu.ukzn.ac.za, [2]afullot@ukzn.ac.za, [3]alongea@ukzn.ac.za

Abstract: The knowledge of adequate rainfall statistics will contribute greatly to the roll-out of emerging wireless technologies on the platform of Long-Term Evolution (LTE) and WiMax (IEEE 802.16). Therefore, it is important that rainfall measurements at shorter integration time are incorporated as useful inputs in the planning of Line-of-Sight (LOS) microwave and millimetre communication links for hosting these technologies. As compared to the use of one-minute rainfall data as suggested by International Telecommunication Union (ITU), the equivalent data measured at 30-second interval gives more information of temporal rain rates in the time domain. Therefore, in this study, rainfall rate measurements of 5-minute integration time representative of 10 locations in South Africa are evaluated to obtain their cumulative distributions. Results from these analyses are compared with rainfall data of one-minute and 30-second integration time data obtained over Durban (29°52'E, 30°55'S), South Africa. Consequently, rainfall rate models for conversion to one-minute and 30-second integration times were obtained over 10 locations in South Africa using the power-law regression functions. Our results obtained over these locations were used to estimate specific attenuation values in selected microwave and millimetric wave bands at 12 GHz, 30 GHz and 60 GHz for 10 locations under study. It is confirmed that the 30-second integration time provides more information needed for estimation of specific attenuation on microwave and millimeter-wave radio links in South Africa.

Key words: Rainfall rate, integration time, rainfall rate conversion factors, specific attenuation

1. INTRODUCTION

Rain-induced attenuation is of great concern to microwave communication system engineers especially at frequencies above 10 GHz [1, 2]. These higher frequencies are utilized by internet service providers (ISPs), online broadcast companies, local multipoint distribution systems (LMDS), as well as satellite networks owing to their high capacity data rate [2, 3]. During the planning, design and implementation of satellite and terrestrial millimetric wave links and systems, sufficient information on rainfall attenuation is required for the location under consideration. This information can be projected by analysing data that has been collected over a period of time over that location, [1–4]. There is a general agreement that rainfall data with lower integration times provides more information for accurate prediction of rainfall attenuation. This is largely due to improved time series resolution of rainfall events which is often necessary to track massive fluctuations in rainfall attenuation. Subsequently, measured data at lower integration times such as one minute or lower become very useful for effective prediction of rainfall effects over radio links at microwave and millimetric wave bands - this information can then be used for effective radio systems design.

Significant research work has been carried out related to rainfall attenuation prediction over South Africa, especially in Durban, for microwave and millimetric wave bands propagation [4-9, 11, 12]. Studies conducted in this region were often centred on seasonal variability of rainfall, rainfall rates and rain drop size distributions. In one of these studies, Odedina and Afullo [7], in their work, suggested rainfall zones for prediction of attenuation based on International Telecommunication Union (ITU) recommendation P.837-4 in [13]. In their work, Odedina and Afullo [7] likewise observed north eastern provinces of South Africa experiences more rain fading compared to the western provinces. Additionally, in his experimental campaign, Owolawi [8] developed rainfall rate contour maps for South Africa's locations for 5-minute to one-minute integration times and this study buttressed the earlier investigations of [7]. Akuon and Afullo [11], using 60-minute and one-minute for Durban, developed conversion factors that could be used by other locations in South Africa to convert their 60-minute data to their equivalent one-minute data. Likewise, [8] developed various rainfall rate conversion methods of Hybrid, Linear, Power and Polynomial functions for conversion of 5-minute data to one-minute integration time over 21 stations in South Africa. Enhancements of rainfall studies were also achieved by rainfall drop size distribution (DSD) approach. In this approach, Alonge

and Afullo [9], with the application of parameter estimation techniques, confirmed that the lognormal and gamma DSDs provided best fits of probability characteristics of drop sizes over Durban. They went further and used this approach to establish seasonal variability of DSDs and their results projected that periods of summer and autumn experience high probabilities of outages in wireless networks over this region. An investigation reveals that overall work done in South Africa has utilized mainly 60-minute and one-minute integration times data [6, 10]. Nevertheless, many researchers have observed that outage prediction analysis for wireless networks require rainfall data with a lower integration time of 30 seconds or less [2, 3, 14]. This observation leads us to undertake this study.

With regard to integration times of less than 60-minute, most research papers have utilized 15-minute, 10-minute and 1-minute data. [3, 8]. Nevertheless, these integration time data are scarce in most parts of the world. Due to this scarcity, radio systems designers may have no option but to estimate rainfall attenuation from processed 60-minute data that is available – though this is not encouraged due to underestimation of rainfall attenuation. It has been observed that better time series of rainfall rate variations are usually obtained from rainfall measurements with less than 60-minute sampling time. Information resulting from these shorter sampling time data is important for radio engineers for determination of sufficient fade margins to overcome rainfall attenuation effects in millimetric wave bands [4, 14]. The main approach for determination of rainfall attenuation for microwaves involves determination of specific attenuation using a power-law function that relates rainfall rate and specific attenuation, [15-17].

National meteorological administrations are indispensable sources of rainfall rate measurements. These administrations archive measured rainfall data that is collected over relatively long periods of time. Alternatively, rainfall rate measurements can also be obtained by carrying out independent measurements using radars, rain gauges or disdrometers with relatively small sampling times [3, 11, 14]. Amongst the three types of measuring instruments, the rain gauge is the most commonly used instrument because it is cost effective and can easily be installed. Different types of rain gauges exist including tipping bucket rain gauges, optical rain gauges, the standard (graduated cylinder) rain gauges, weighing precipitation gauges. When a rain gauge is installed at the surface, it measures the point accumulation of rain-water as rain rate [18].

The Rainfall data collected over Durban was obtained from the disdrometer and the rain gauge over a period of time. These two equipment have varying levels of accuracy and measurement errors, with the disdrometer having an improved sensitivity to rainfall measurements than the rain gauge [18]. The disdrometer unit has two components: outdoor and indoor units. The outdoor unit consists of a droplet receiving area of 0.005 m^2. It is capable of processing rainfall data into 20 channels via the indoor unit, [19] with each of the channels related to rain drops with diameter, D_i, in the range $0.3\ mm \leq D_i \leq 5.4\ mm$. The rainfall rate, R, is associated to the mean drop diameter, D_i, in the ith class, by [6, 20]:

$$R = \frac{6\pi \times 10^{-4}}{A \times T} \sum_{i=1}^{20} {D_i}^3 C_i \quad [mm/h] \tag{1}$$

Where:

C_i = the number of rain drops in the ith class
T = the sampling time given as 60 seconds
$v(D_i)$ = the terminal velocity of rain drop in m/s
A = the sampling area given as 0.005 m^2

Conversely, the operation of the tipping rain gauge uses a different measurement principle during measurements of rainfall rates. The tipping sequence is signalled when a reed sensor is triggered. The rain gauge has a poor sensitivity especially at very low rainfall rates (< 2 mm/h), but, on the other hand, it gives a more inexpensive way of collecting rainfall data across the world.

This paper is divided into sub-sections as follows: Section 2 discusses measurements and data processing; in Section 3, we discuss rainfall cumulative distributions and resultant conversion factors generated over Durban; Section 4 presents the application of conversion factors over Durban for generation of conversion factors in other 9 locations of South Africa; Section 5 discusses results associated with specific attenuation and Section 6 provides the conclusion of this study.

2. DATA ACQUISITION

Rainfall data measurements were obtained from the Joss-Waldvögel (JW) RD-80 disdrometer installed at the University of KwaZulu-Natal, Durban, and the rain gauge data obtained from the South African Weather Service (SAWS). Using rainfall data collected over Durban, inferences are made using rainfall rate cumulative distributions in conjunction with their conversion factors. A summary of data measurements are given in Table 1.

Table 1. Rainfall Data Measurements

Integration Time	Duration (Months)
30 seconds	24
1 minute	27
5 minute	132

3. RAINFALL RATE CUMULATIVE DISTRIBUTION AND CONVERSION FACTORS OVER DURBAN

In this section, analysis of rainfall data measurements at different integration times over Durban are done with the aim of obtaining their cumulative distributions. Furthermore, regression analysis is employed to determine relationships between data at different integration times. For optimal wireless network service in a medium affected by rain, cumulative distributions represents an evaluation technique that can be used to identify the percentage of exceedance probability of rainfall rate. These probabilities enable communication systems design experts to define acceptable fade margin levels required by base stations in the reduction of network outages during rainy periods. Generally, a rainfall rate value corresponding to 0.01% exceedance (or 99.99% rainfall availability), is of major interest for sustainability of satellite and terrestrial communication links. This important parameter is frequently referred to as $R_{0.01}$ and is measured in mm/h. Fig. 1 shows cumulative distributions that are obtained for three categories of rainfall rate integration times over Durban.

3.1 Rainfall cumulative distributions for different integration times over Durban

In Fig. 1 and Table 2, we present cumulative distributions for three different integration times measured over Durban, for rainfall rates exceeded with probability, P, where $0.004\% < P < 9.5\%$. Similarly, in Table 2, a summary of rain rate values at different integration times for percentages of rainfall rates exceeded between 0.01% and 1% are presented. Observations from Fig.1 show that the 30-second cumulative distribution is above the one-minute distribution with a margin of 4.8 mm/h at 99.99% system availability requirement. This is a vital source of information because this part of the graph is the high system availability region that suffers greatly from rainfall attenuation. This further confirms that 30-second integration time data provides more information required for computation of rainfall attenuation compared to one-minute data. It is thus manifested in Fig. 1 that the rainfall rate increases as the integration time decreases. This also confirms that a rainfall rate measuring instrument with a long integration time will not capture shorter peaks present in the high rain intensity, resulting to lower measured rainfall intensities per unit length of time.

As observed from Table 2, it is revealed that R_1 value for 30-second integration time is 6.5 mm/h, $R_{0.1}$ is 24.7 mm/h and $R_{0.01}$ is 64.3 mm/h. For one-minute integration time, corresponding values are 5.8 mm/h, 23.2 mm/h and 59.5 mm/h at 1%, 0.1% and 0.01% probability of rainfall rate exceeded, respectively. For 5-minute integration time, rainfall rates are 3 mm/h, 16.8 mm/h and 55.2 mm/h at the same probabilities of exceedance.

From these results, it is observed that $R_{0.01}$ determined over Durban, though lower for one-minute integration time is comparable to the predicted value of 63 mm/h in ITU-R P.837-1[10] for this region.

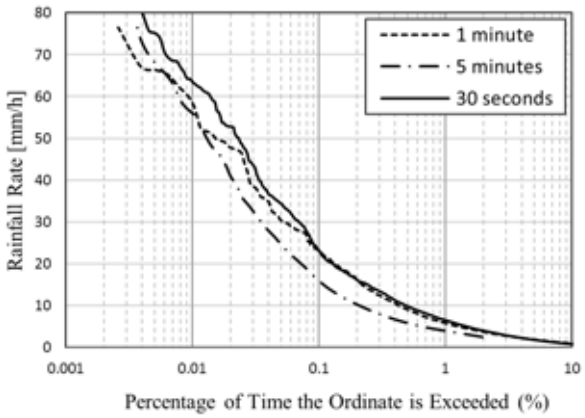

Figure 1: Cumulative distributions from measured rainfall rates for different integration times

Table 2. Measured Rain Rate exceeded for various integration times

Int. Time (sec)	Percentage of time rainfall rate is Exceeded (%)				
	1	0.3	0.1	0.03	0.01
30	6.5	13.6	24.7	43.9	64.3
60	5.8	12.5	23.2	38.3	59.5
300	3.0	8.5	16.8	32.0	55.2

3.2 Determination of rainfall rate conversion factors over Durban

Rainfall rate conversion models exist for conversion from higher integration time rainfall rates, $R_{(T\ \mathrm{min})}$, to one-minute integration time rainfall rates, $R_{(1\ \mathrm{min})}$ [8, 14, 21, 22]. This conversion is beneficial in the development of rain rate models that can be applied in the prediction of rainfall attenuation for a given region, [3, 23]. Among existing models, Matricciani [21] proposes a more mathematical approach that aims at resolving errors present in the T-min probability distribution (PD). These errors include upward translation and clockwise rotation of the T-min PD at a fraction of time, $P\%$, where $P > 1$. In this study, we opt to use the power-law relationship method due to its simplicity and ability to provide of useful information in modelling.

A power law relationship relating rainfall rate at the required integration time, τ, and rainfall rate at available integration time, T, at equal probabilities of exceedance, exists. This relationship was established by Ajayi and Ofoche [2], and is given by:

$$R_\tau = u(R_T)^v \quad [mm/h] \qquad (2)$$

Where:

R = the rainfall rate
u = conversion variable
v = conversion variable

Using specialized database of high resolution rainfall data over 47 stations in Canada, Segal, [24] proposed a method of conversion that was expressed as the proportion of equally probable rainfall rates, in the form:

$$\rho_\tau(P) = \frac{R_1(P)}{R_\tau(P)} \quad (3)$$

and

$$\rho_\tau(P) = aP^b \quad (4)$$

Where:

$\rho_\tau(P)$ = the conversion factor
$R_1(P)$ = rainfall rate at one-minute integration time
$R_\tau(P)$ = rainfall rate τ-minute integration time
P = equal probability of occurrence
a = regression coefficient
b = regression coefficient

There are two main approaches used for rain rate conversion - use of equivalent rainfall rates or application of the same probability of rainfall rate occurrence [25]. The method adopted in this paper is the equal probability method. Using 5-minute, one-minute and 30-second data collected over Durban, conversion factors for conversion from higher to lower integration times were generated using the power-law fit and are shown in Fig. 2 (a) - (c). Subsequently, these conversion factors are compared to those obtained by other researchers in different parts of the world

Determination of conversion factors for one-minute integration time: Using (2) and regression fitting shown in Fig. 2, one-minute rainfall conversion coefficients as determined for the location of Durban is given in (5) as:

$$R_1 = 1.964\left(R_{5,DBN}\right)^{0.858} \quad [mm/h] \quad (5)$$

Where:

R_1 = one-minute integration time
R_5 = 5-minute integration time

Results of Table 3 show comparison of regression coefficients u and v obtained over Durban at one-minute integration time with those obtained by Flavin [26] in Australia, USA, Europe and Canada and Ajayi and Ofoche [3] over Ile-Ife in Nigeria. Observations show that the coefficient u in the proposed model for Durban is

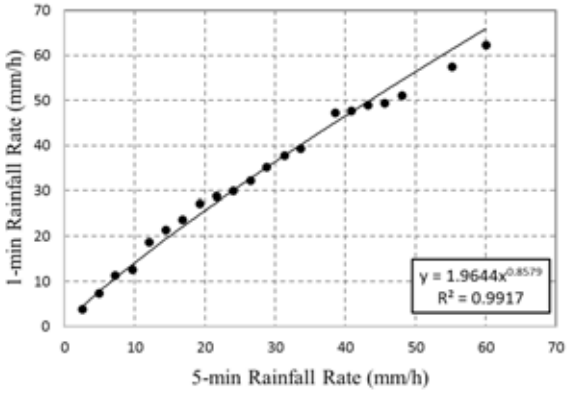

Figure 2: Power-law fits for determination of coefficients u and v for Durban in conversion from 5-minute to one-minute integration time

Table 3. Comparison of Durban's u and v coefficients power-law coefficients with other models

Model	$R_\tau = u(R_T)^v$ for τ = 1 min				Error (%)
	T (min)	u	v	$R_{0.01}$	
AJAYI [3]	5	0.991	1.098	81.0	36.1
OWOLAWI [7]	5	1.062	1.051	71.9	20.8
FLAVIN [25]	6	0.990	1.054	67.9	14.1
Proposed	5	1.964	0.858	61.3	3.0

higher than its counterparts from other locations of the world. From error analysis Ajayi and Ofoche [3] model resulted in an error of 36.1%, the Owolawi [8] model gave error of 20.8%, Flavin [26] model gave 14.1% and the proposed model in (5) produced an error of 3.0%. The highest error is thus observed from Ajayi and Ofoche [3] model. The tropical climate of Ile-Ife, characterized by heavy rainfall may be one factor contributing to this large error, bearing in mind that Durban is mainly subtropical.

From Table 3, it is observed that the Flavin [26] model is closer to the measurements in Durban with an error of 14.1%.

Determination of conversion factors for 30-second integration time: Rainfall rate conversion models from 5-minute and one-minute data to 30-second data were determined using regression fittings in Fig. 3(a) and Fig. 3(b):

$$R_{30s} = 2.078\left(R_{5,DBN}\right)^{0.868} \quad [mm/h] \quad (6)$$

$$R_{30s} = 1.051\left(R_{1,DBN}\right)^{1.004} \quad [mm/h] \quad (7)$$

Where:

R_{30s} = the rainfall rate in mm/h at 30-second integration time
R_1 = one-minute integration time rainfall rates

R_5 = 5-minute integration times rainfall rate

It observed from Table 4 that predicted 30-second rainfall rates are higher than measured one-minute and 5-minute rainfall rates and especially at 99.99% system availability requirement. There is a margin of 4.1 mm/h rainfall rate between these two integration times.

Similarly, predicted rainfall rate at 30-second from 5-minute data is 67.6 mm/h, up from a measured value of 55.2 mm/h at 5-minute integration time.

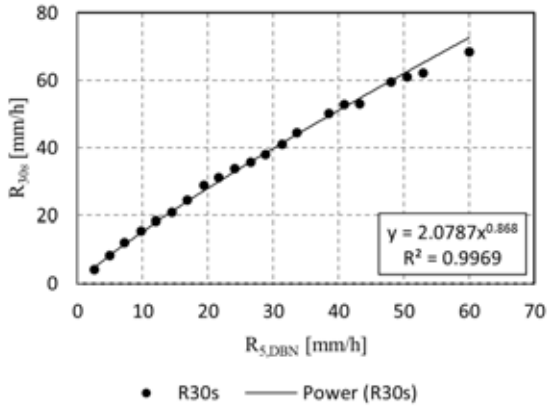

(a)

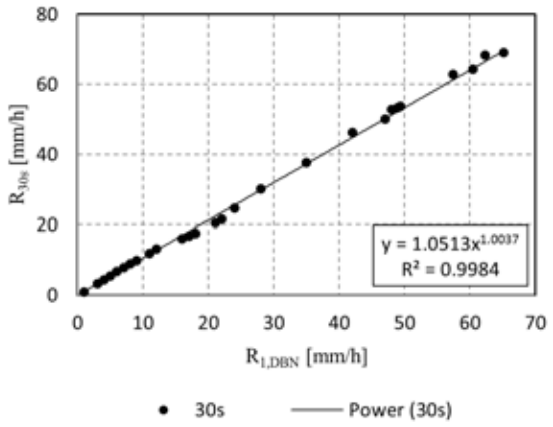

(b)

Figure 3: Power-law fit for determination of coefficients *u* and *v* for Durban in conversion to 30-second from (a) 5-minute (b) one-minute data

Table 4: Predicted rainfall rates at 30-second integration time

Int.Time (T sec)	$R_\tau = u(R_T)^v$ [mm/h], for τ = 30s				
	R_1	$R_{0.3}$	$R_{0.1}$	$R_{0.03}$	$R_{0.01}$
60	6.1	13.3	24.7	40.8	63.6
300	5.4	13.3	24.1	42.1	67.6

3.3 Error analysis and validation of proposed power-law models over Durban

Estimates from our proposed rainfall rate conversion models should be representative of actual measurements. In this regard, our models in (5) - (7) were validated using Root mean Square Error (RMSE) and the Chi squared statistics (χ^2) test for goodness of fit. Expressions that were used for computation of errors are given in (8) and (9) [27]:

$$RMSE = \sqrt{\frac{1}{N}\sum_{k=1}^{k}[y_k - f(x_k)]^2} \quad (8)$$

$$\chi^2 = \sum_{k=1}^{k}\frac{\left(y_k - f(x_k)\right)^2}{y_k} \quad (9)$$

Where:

y_k = measured rainfall rate
$f(x_k)$ = predicted respectively
N = sample size.

In Table 5, we present a summary of results obtained from error analysis in (8) and (9) for power-law models describing our conversion models.

The chi-squared test was carried out at a confidence level of 0.05 and gave values of 2.037, 0.845, and 1.0193, for the three models in (5) - (7), respectively. A comparison with the chi-squared table shows that proposed rainfall rate conversion models passed the test and can be used for future conversions in Durban.

Table 5. Power-Law conversion coefficients for three models over Durban

***T* (Sec)**	$R_\tau = u(R_T)^v$ for τ = 60s			Error analysis	
	u	***v***	**R^2**	RMS	CHI
300	1.964	0.858	0.992	1.883	2.037[a]
	$R_\tau = u(R_T)^v$ for τ = 30s				
300	2.078	0.868	0.997	1.324	0.845[b]
60	1.051	1.004	0.998	1.051	1.019[c]

Significant level is given as [a]32.671, at DF = 21, [b]32.671 at DF = 21, and [c]40.113 at DF = 27

Comparisons of proposed models: Durban's one-minute measured rainfall data were compared with selected global models including the Moupfouma and Martin [28] model, the Rice-Holmberg (R-H) [29] model and ITU-R P.837-1[10] model, as shown in Fig. 4. This figure shows

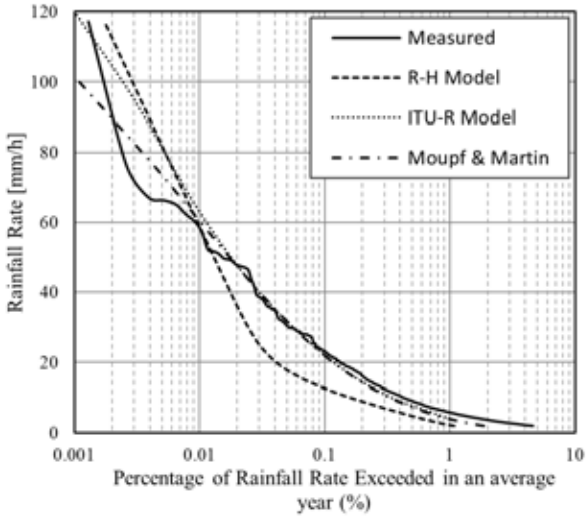

Figure 4: Comparisons of measured and predicted data over Durban with other models

Table 6. Comparison of one-minute Rainfall rates over Durban with other global models

Model	Rainfall rates [mm/h]			RMS (%)
	R_1	$R_{0.1}$	$R_{0.01}$	
Measured (Durban)	5.8	23.1	59.5	-
Moupfouma and Martin	3.9	22.0	59.5	-
R-H Model	2.3	12.6	60.3	1.3
ITU-R Model (Zone M)	4.0	22.0	63.0	5.9

a comparison of measured and predicted rainfall intensities exceeded in a fraction of a year. It is seen from Fig. 4 and Table 6 that the predicted values by other models agree quite well with the measured values. These models predict a rainfall rate of around 60 mm/h at 0.01% exceedance, which is relatively close to proposed $R_{0.01}$ value of 63 mm/h for Durban in region M, [10]. It is also noted that the R-H model overestimates rain rates from 0.004% and below when it is compared with measured values, and this supports Crane's observations that this model overestimates rain rates from 0.01% and lower [14].

Predicted values were compared with the Durban's measured $R_{0.01}$ of 59.5 mm/h and RMS errors show that R-H model is closest to the measured value with an error of 1.3%.

4. DEVELOPMENT OF RAINFALL CONVERSION FACTORS FOR OTHER LOCATIONS IN SOUTH AFRICA

Due to scarcity of, especially one-minute or lower rainfall rates in other locations of South Africa, conversion models developed in (5) and (6) over Durban were used to convert 5-minute rainfall data available in other locations to their equivalent one-minute and 30-second. All geographical locations under study, representing eight out of nine provinces of South Africa, were categorized according to Köppen-Geiger classification as presented in Table 7. Based on earlier research by Köppen and Geiger, [30], the Council for Scientific and Industrial Research (CSIR) created a new Köppen-Geiger classification map for South Africa, [31]. This classification is a 2- or 3-letter code that describes the climatic characteristics of a region by considering a combination of precipitation and temperatures. For instance, a climate described as **Cfa** is a warm temperate climate, fully humid with hot summers and temperatures, $T_{max} \geq +22°C$. A **Csc** is a warm temperate climate with dry and cool summer and cold winter seasons. Winter temperatures drop to as low as -38°C. A **Cwb** climate is warm temperate with dry winter and warm summer seasons with average monthly temperatures of +10°C. The **Bs** code denotes steppe climates with **Bsh** denoting a hot steppe with annual temperatures, $T_{ann} \geq +18°C$. The **BWh** is a hot steppe/desert climate with annual temperatures $T_{ann} \geq +18°C$.

Table 7. Geographical description of locations in this study

LOC.	Coordinates		Köppen-Geiger Classification [31]	
	LONGT.	LAT.	Class	Description
BET	28.23ºS	28.30ºE	Cwb	Temperate
BLM	29.12ºS	26.23ºS	Bsk	Steppe
CTN	33.93ºS	18.42ºS	Csc	Temperate
DBN	29.88ºS	31.05ºS	Cfa	Sub-tropical
ELD	32.98ºS	27.87ºS	Cfa	Sub-tropical
IRN	25.87ºS	28.22ºS	Cwb	Temperate
MFK	25.85ºS	25.63ºS	BSh	Steppe
MSB	34.18ºS	22.13ºS	Bsk	Steppe
PLK	23.90ºS	29.45ºS	Bsk	Steppe
UPT	28.40ºS	21.27ºS	BWh	Desert

Key:

Acronym	Name	Acronym	Name
BET -	Bethlehem	IRN -	Irin
BLM -	Bloemfontein	MFK -	Mafikeng
CTN -	Cape Town	MSB -	Mossel Bay
DBN -	Durban	PLK -	Polokwane
ELD -	East London	UPT -	Upington

4.1. Empirical distributions for 10 locations in South Africa at 5-minute integration time

Empirical rain rate distributions for different climatic locations within South Africa at 5-minute integration time are presented in Fig. 5. These distributions show probabilities of occurrences of rainfall rate distributions of specified intensities for each location. A summary of measured rainfall rates are summarized in Table 8.

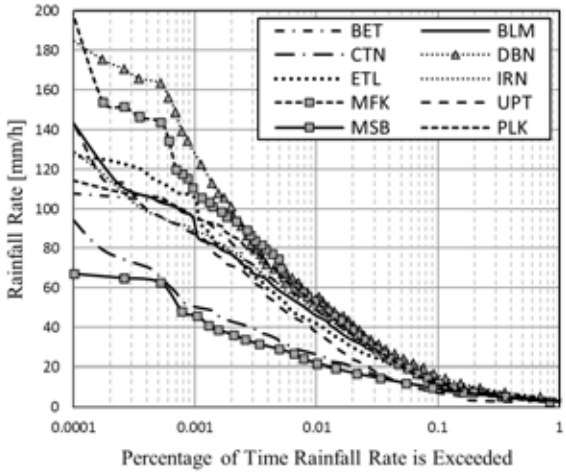

Figure 5: Cumulative distributions for 10 locations at 5-minute integration time

Table 8. Measured Rainfall Rate Intensities at 5-minute Integration Time

Loc.	Rainfall rates [mm/h]				*M* [mm]
	R_1	$R_{0.1}$	$R_{0.01}$	$R_{0.001}$	
BET	2.5	12.0	48.0	96.0	624.0
BLM	2.5	12.0	45.6	96.0	507.7
CTN	3.0	8.0	26.0	50.5	464.0
DBN	4.0	16.0	55.2	130.0	889.0
ELD	3.5	13.0	41.0	105.0	830.7
IRN	2.8	12.0	48.0	88.0	581.5
MFK	2.3	12.0	52.9	110.4	470.0
MSB	2.7	9.7	21.6	45.6	403.6
PLK	2.6	12.0	51.0	96.0	426.0
UPT	2.1	7.2	36.0	86.4	229.2

As observed in Fig. 5 and Table 8, Durban recorded higher values of rainfall rates exceeded at 0.002% and below compared to other locations, followed by Mafikeng. In the lower end is Mossel Bay and Cape Town with low rainfall rates at the same probability of exceedance. Also, it is observed from Table 8 that there is no obvious correlation between mean annual rainfall and rainfall exceeded for a percentage of time. As an example, East London recorded the second highest annual mean rainfall of 830.7 mm, yet its $R_{0.01}$ rainfall rate was only 41 mm/h as compared with Polokwane's $R_{0.01}$ value of 51.0 mm/h with an annual mean rainfall of 426.0 mm. One explanation for this could be that Polokwane receives heavy rains of convective type within short periods as compared with East London that experiences lighter rains of stratiform type for relatively longer periods. Also, other topographical features, including hills, water masses and presence of mountains, may influence the rain climate of a region.

Observations from Table 8 also affirms Köppen-Geiger classification map for South Africa. For instance, it is observed that Cape Town, with a **Csc** climate, has a relatively low $R_{0.01}$ rainfall rate of 26.0 mm/h. Cool summers, in this location, experience low amounts of precipitation contributed by less evaporation due to low temperatures. Correspondingly, Durban, classified with a **Cfa** climate, recorded higher rainfall rates of 55.2 mm/h compared with other locations.

4.2. Analysis of rainfall rate conversion factors for other locations in South Africa

Available 5-minute data in 9 other locations in conjunction the 5-minute, one-minute and 30-second data available in Durban, led to development of conversion models for other locations. Following a confirmation drawn from Table 3 that lower integration time data provide more information on rainfall statistics of a location as compared with a higher integration time data, it was deemed necessary to generate conversion factors for other locations to obtain lower integration time data.

Determination of conversion factors for conversion to one-minute integration time: Having obtained useful rain rate values from 5-minute cumulative distributions from selected locations, it is most important to convert these values to values of lower integration as undertaken in [8] and [11]. Akuon and Afullo [11] proposed a mathematical technique of executing this by comparing and substituting the values from rain conversion power-law functions. Firstly, parameters for other locations were determined using the power-law function proposed by [32], [33]:

$$R_1(P) = \mu[R_\tau(P)]^\lambda \qquad [mm/h] \tag{9}$$

Where:

R_1(P) = one-minute rainfall rates exceeded for a percentage P of the year

R_τ(P) = τ-minute rainfall rates exceeded for a percentage P of the year

μ and λ = regression coefficients.

Making use of (1), conversion factors for Durban were determined as seen in (10),

$$R_{1,DBN} = \mu\left(R_{5,DBN}\right)^\lambda \qquad [mm/h] \tag{10}$$

Where:

μ and λ = conversion factors obtained for Durban.

The 5-minute equiprobable rainfall rates at each of the 9 locations were used in the determination of regression factors, [11], using (11),

$$R_{5,Y} = \phi\left(R_{5,DBN}\right)^\beta \qquad [mm/h] \tag{11}$$

Where:

$R_{5,Y}$ = 5-minute equivalent of Durban's 5-minute at region Y
ϕ and β = regression factors for region Y.

Consequently, from (9) - (11), conversion factors from 5-minute data to one-minute data for Location Y in South Africa, can be determined using (12), [11]:

$$R_{1,Y} = \mu\left(\phi\left(R_{5,DBN}\right)^{\beta}\right)^{\lambda} \equiv m\left(R_{5,DBN}\right)^{n} \; [mm/h] \quad (12)$$

Where:

$R_{1,Y}$ = the derived one-minute equivalent rainfall rate for location Y
$\mu, \lambda, \phi, \beta, m$ and n = regression coefficients

and

$$m = \mu\phi^{\lambda} \quad (13a)$$

$$n = \beta\lambda \quad (13b)$$

with μ = 1.9644, λ = 0.858 over Durban and values of ϕ and β as given in Table 9.

Consequently, results of the application of the model in (12) to other 9 locations are presented in Table 9.

Determination of conversion factors for conversion from 5-minute to 30-minute integration time: Applying the same concept, used in (10) – (12), a conversion model for conversion from 5-minute data to 30-second data is given as [11]:

$$R_{30s,D} = \phi\left(R_{5,DBN}\right)^{\theta}, \qquad [mm/h] \quad (14)$$

and,

$$R_{30s,Y} = \varphi\left(\phi\left(R_{5,DBN}\right)^{\beta}\right)^{\theta} \equiv p\left(R_{5,DBN}\right)^{q} [mm/h] \quad (15a)$$

Where:

$R_{30,Y}$ = the equivalent 30-seconds rainfall rates for location Y
p and q = regression coefficients

and

$$p = \varphi\phi^{\theta} \quad (15b)$$

$$q = \beta\theta \quad (15c)$$

Table 9. Factors for Conversion from 5-minute data to one-minute data

LOCATION	$R_{5,DBN} \rightarrow R_{5,Y}$		$R_{5,DBN} \rightarrow R_{1,Y}$	
	ϕ	β	m	n
BET	0.910	0.968	1.8117	0.8305
BLM	0.893	0.966	1.7826	0.8288
CTN	0.777	0.875	1.5820	0.7508
ELD	0.970	0.943	1.9137	0.8091
IRN	1.141	0.918	2.1998	0.7876
MFK	0.727	1.057	1.4943	0.9069
MSB	0.951	0.800	1.8815	0.6864
PLK	0.645	1.066	1.3484	0.9146
UPT	0.289	1.191	0.6771	1.0219

Table 10. Conversion factors for conversion from 5-minute data to 30-second data

LOCATION	$R_{30s} = p\left(R_{5,DBN}\right)^{q}$ $[mm/h]$	
	p	q
DBN	2.0780	0.8680
BET	1.9147	0.8402
BLM	1.8836	0.8385
CTN	1.6693	0.7595
ELD	2.0238	0.8185
IRN	2.3301	0.7968
MFK	1.5756	0.9175
MSB	1.9893	0.6944
PLK	1.4202	0.9253
UPT	0.7075	1.0338

with φ = 2.0780, θ = 0.8680 over Durban and values of ϕ and β as given in Table 9 for other locations.

In Table 10, we present conversion factors for different climatic locations in South Africa as processed from 11-year, 5-minute integration time data. From this table, it may be deduced from these coefficients that Durban has higher rainfall rates than other locations under study at the same probability of exceedance.

Rainfall rate cumulative distribution for 10 locations in South Africa: Cumulative distributions over various locations in South Africa at one-minute and 30-second predicted data are presented in Fig. 6 (a) and (b). Observations show that predicted data at 30-second integration time are higher than at one-minute integration time, as expected.

Fig. 6 and Table 11 presents predicted rainfall rates at one-minute and 30-second integration times after application of conversion models in (12) and (15). Observations from this table reveals that rainfall rates at 30-second integration time are higher than those at one-minute integration time at same probability of exceedance. Generally, there is an average margin of 0.95 mm/h at 99% system availability between one-minute and 30-second rainfall rates when all 10 locations

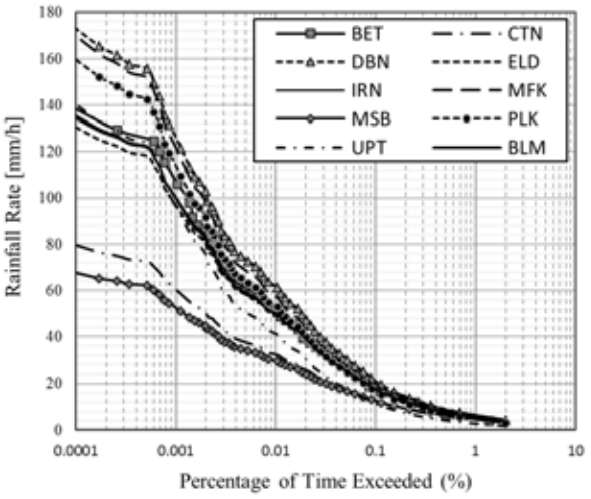

(a)

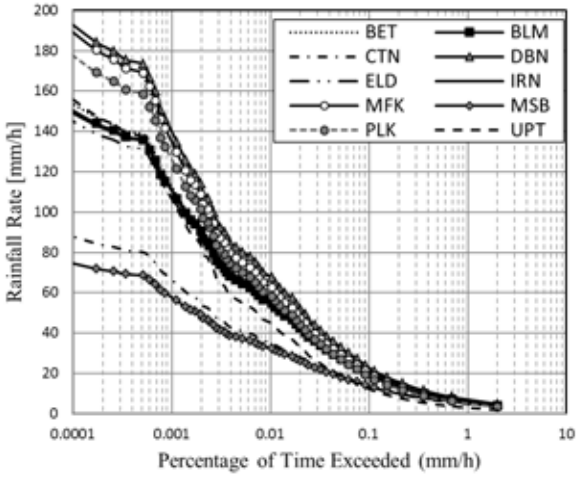

(b)

Figure 6: Cumulative distributions for 10 locations for predicted rainfall rates at (a) one-minute and (b) 30-second integration times

Table 11. Predicted one-minute and 30-Second Rainfall Rates for 10 Locations in South Africa

Loc.	Rainfall rates [mm/h]					
	$R_{1,Y}$			$R_{30s,Y}$		
	R_1	$R_{0.1}$	$R_{0.01}$	R_1	$R_{0.1}$	$R_{0.01}$
BET	4.5	17.0	50.7	6.3	19.5	55.7
BLM	4.5	16.3	49.5	6.0	19.2	54.4
CTN	3.2	11.7	32.1	4.8	13.6	35.1
DBN	5.8	20.3	61.3	6.8	23.0	67.6
ELD	5.5	17.7	49.1	6.3	19.5	53.9
IRN	5.7	19.2	51.8	7.1	20.1	56.9
MFK	5.6	16.8	56.8	5.8	19.9	62.5
MSB	4.2	11.7	29.5	5.2	13.6	32.2
PLK	5.2	17.8	52.9	5.2	18.4	58.1
UPT	2.8	10.3	40.8	3.0	12.4	44.7

are considered. In the same way, the margins are 2.04 mm/h and 4.66 mm/h at 99.9% and 99.99% system availability requirements, respectively. The higher margin at high system availability requirement buttresses the need for using rainfall rate measuring equipment with lower integration times for data collection.

Error analysis of proposed power-law models: Owing to lack of measured one-minute data for other locations under study, one-minute predicted values are compared with [34] proposed one-minute rainfall rate exceedance values. Table 12 shows predicted rainfall rate intensities exceeded at one-minute integration time compared to ITU-R P.837-6 proposed valuesfor 0.01% of the average year for each of these locations. The lowest deviation error of -1.0% was observed from the proposed model for Bloemfontein, whereas the highest error of 5.8% is observed in the model proposed for Polokwane. Nevertheless, it is observed that predicted values are comparable to ITU-R values with some slight deviations. This is expected because the empirical measurement analysis gives more accurate values of rainfall intensities for a particular location under study as opposed to regional values that are more generalized. These deviations may be caused by variations in climatic conditions from one location to another within the same region.

5. SPECIFIC ATTENUATION PREDICTION FOR 30-SECOND INTEGRATION TIME OVER SOUTH AFRICA

The fast growing need for high capacity and high speed links for wireless communications is pushing network service providers towards utilization of Ku, Ka and V bands for both terrestrial and satellite communications. Services that need high channel capacity include multipoint video distribution services (MVDS), wireless broadband access (WBA) and other broadband services [1].

The major obstacle in operating at high frequency-bands is signal attenuation caused by electromagnetic wave absorption and scattering in high intensity rainfall rates. An empirical procedure based on the power-law function relating rainfall rate and specific attenuation as proposed by [16] is applied in this section. Specific attenuation values were determined at Ku, Ka and 60 GHz bands as shown in Fig. 7. The 60 GHz channel is an unlicensed band that has been identified for use in short range wireless communications due to its high speed capability and frequency reuse [35]. ITU-R P.838-3 [16] provides a systematic guide in the calculation of specific attenuation, γ_R, for one-minute rainfall on the link as:

$$\gamma_R = kR_1^{\alpha} \quad [dB/km] \tag{16}$$

Where:
R = rain rate in mm/h
k and α = are frequency and polarization dependent coefficients, usually provided by ITU-R P.838-3 [16].

By following the assumption that values of k and α in (16) are wholly frequent-dependent, as deduced in the technical publication of ITU-R P.838-3 [16], it then logically follows from the earlier procedure in (9)-(13) that the equivalent computation of specific attenuation for 30-seconds rainfall rate over any location in South Africa is given as:

$$\gamma_{R,30s} = k(xR_{30}{}^{y})^{\propto} \quad [dB/km] \tag{17}$$

Where:

x and y = required power-law coefficients for conversion of 30-second rainfall data to one minute as obtained over the investigated locations.

A set of coefficients for three frequencies are given in Table 13. Specific attenuation values were estimated at one-minute integration time at Ku (12 GHz), Ka (30 GHz) and 60-GHz bands and are presented in Fig. 7 and Table 13 for all locations under study.

Observations from Table 14 indicate that, for instance, there is need to allocate more fade margins for communication links over Durban than Mossel Bay over the same link length. Otherwise, communication links over Durban need to be shorter than those at Mossel Bay at the same frequency. Another observation drawn from this table shows that predicted specific attenuation values using horizontal polarization, are higher than those obtained when using vertical polarization. For instance, there is general average margin of 0.45 dB/km at 12 GHz, 1.56 dB/km at 30 GHz and 1.24 dB/km at 60 GHz for one-minute rainfall at the considered locations in South Africa. However, the trend observed for predictions over 30-second are 0.50 dB/km, 1.76 dB/km and 1.3 dB/km respectively. This suggests that specific attenuation at 30-seconds integration time requires a slightly higher margin to achieve rain fade mitigation at all these locations.

Table 12. Comparison of predicted one-minute $R_{0.01}$ rainfall rates with ITU-R proposed values

Loc.	$R_{1,Y}$	ITU-R	Deviation (%)
BET	50.7	50	1.4
BLM	49.5	50	-1.0
CTN	32.1	30	7.0
DBN	61.3	63	-2.7
ELD	49.1	50	-1.8
IRN	51.8	50	3.6
MFK	56.8	60	-5.3
MSB	29.5	30	-1.7
PLK	52.9	50	5.8
UPT	40.8	40	2.0

Table 13. Frequency-dependent coefficients for estimation of specific rain attenuation as provided by ITU-R [16]

FREQ. (GHz)	k_H	$\propto_H$	k_V	$\propto_V$
12	0.0236	1.1825	0.02455	1.1216
30	0.2403	0.9485	0.2291	0.9129
60	0.8606	0.7656	0.8513	0.7486

Table 13. Frequency-dependent coefficients for estimation of specific rain attenuation as provided by ITU-R [16]

FREQUENCY (GHz)	k_H	$\propto_H$	k_V	$\propto_V$
12	0.0236	1.1825	0.02455	1.1216
30	0.2403	0.9485	0.2291	0.9129
60	0.8606	0.7656	0.8513	0.7486

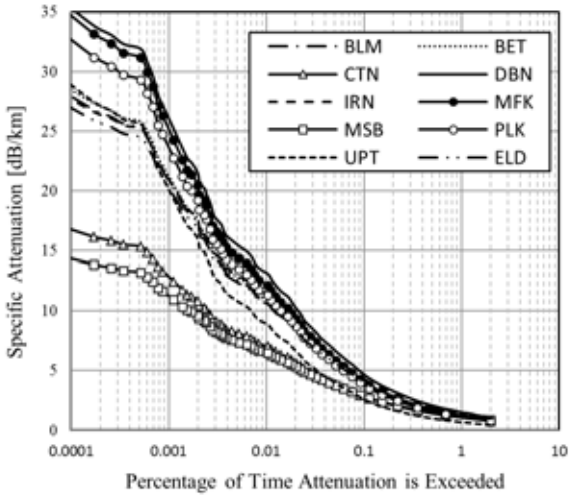

(a)

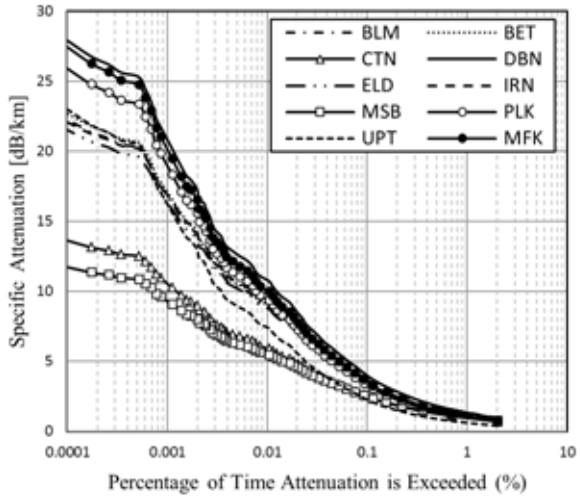

(b)

Figure 7: Computed specific attenuation exceeded for different percentages of time at one-minute integration time data over South Africa at 30 GHz Band for (a) Horizontal polarization (b) vertical polarization

Also, it is confirmed that specific attenuation due to rainfall increases as frequency of operation increases, as expected. This implies that a consequent increase or decrease in rainfall rate also affects the system availability. As a result, the occurrence of high rainfall rate in Durban will affect the performance of radio links.

6. CONCLUSION

Rainfall rate conversion models for conversion to one-minute and 30-second integration time data for other locations with 5-minute integration time data were developed using available 5-minute, one-minute and 30-second integration time data over Durban. Application of developed conversion models has demonstrated that rainfall rates at lower integration time are comparably higher, providing the much needed information by microwave link designers for the fulfilment of reliable links with optimum availability. Comparison of developed models with other proposed models in other parts of the world showed a general trend of agreement. Measured and predicted one-minute data obtained over Durban were found to be comparable to ITU-R P.837-1 predicted value of 63 mm/h for Durban, South Africa. Specific attenuation values computed based on one-minute and 30 second rainfall rates over South Africa reveal that more fade margins are required for areas that experience higher rainfall rates.

Table 14. Predicted Specific Attenuation calculation over South Africa using (16) and (17) at 99.99% system availability requirements

LOC.	*f*req. (GHz)	H_{1min}	H_{30s}	V_{1min}	V_{30s}
BET	12	2.48	2.77	2.01	2.23
	30	9.95	10.9	8.25	8.99
	60	17.4	18.7	16.1	17.3
BLM	12	2.41	2.69	1.95	2.17
	30	9.73	10.6	8.07	8.8
	60	17.1	18.3	15.8	17
CTN	12	1.44	1.6	1.2	1.33
	30	6.45	7.02	5.44	5.9
	60	12.3	13.1	11.4	12.2
DBN	12	3.1	3.47	2.48	2.77
	30	11.9	13.1	9.81	10.7
	60	20.1	21.6	18.5	19.9
ELD	12	2.38	2.67	1.94	2.15
	30	9.65	10.6	8.01	8.74
	60	17	18.2	15.7	16.9
IRN	12	2.54	2.85	2.06	2.29
	30	10.2	11.1	8.41	9.2
	60	17.7	19	16.4	17.6
MFK	12	2.83	3.18	2.28	2.54
	30	11.1	12.2	9.15	10
	60	19.0	20.4	17.5	18.8
MSB	12	1.31	1.45	1.09	1.21
	30	5.95	6.49	5.03	5.47
	60	11.5	12.3	10.7	11.5
PLK	12	2.60	2.92	2.10	2.34
	30	10.4	11.3	8.58	9.36
	60	18.0	19.3	16.6	17.8
UPT	12	1.92	2.14	1.57	1.75
	30	8.10	8.85	6.77	7.37
	60	14.7	15.8	13.7	14.7

7. REFERENCES

[1] D.L. Emiliani, L. Luini, and C. Capsoni: "Analysis and parameterization of methodologies for the conversion of rain rate cumulative distributions from various integration times to one minute," *IEEE Antennas and Propagation Magazine*, Vol. 51, No. 3, pp. 70-84, June 2009.

[2] G.O. Ajayi and E.B.C Ofoche: "Some tropical rain rate characteristics at Ile-Ife for microwave and millimeter wave applications," *Journal of Climate and Applied Meteorology*, Vol. 23, pp. 562-567, April 1984.

[3] M.R. UI Islam, T.A Rahman, S.K.A. Rahim, K.F. Al-Tabatabaie and A.Y. Abdulrahman: "Fade margins prediction for broadband fixed wireless access (BFWA) from measurements in tropics,"

Progress In Electromagnetics Research C, Vol. 11, pp. 199-212, 2009.

[4] S.J. Malinga, P.A. Owolawi and T.J.O. Afullo: "Computation of rain attenuation through scattering at microwave and millimeter bands in South Africa," *Progress in Electromagnetics Research Symposium Proceedings*, Taipei, pp. 959-971, 2013.

[5] P.A. Owolawi, T.J. Afullo and S.B. Malinga: "Effect of rainfall on millimeter wavelength radio in Gough and Marion Islands," *Progress in Electromagnetics Research Symposium*, Beijing, China, March 23-27, 2009.

[6] A.A. Alonge and T.J. Afullo: "Seasonal analysis and prediction of rainfall effects in eastern South Africa at Microwave Frequencies," *Progress in Electromagnetics Research B*, Vol. 40, pp. 279-303, 2012.

[7] M.O. Odedina and T.J.O. Afullo: "Characteristics of seasonal attenuation and fading for line-of-sight links in South Africa," *SATNAC*, pp. 1-6, 2008.

[8] P.A. Owolawi: "Derivation of one-minute rain rate from five-minute equivalent for the calculation of rain attenuation in South Africa," *PIERS Online*, Vol. 7, No. 6, pp. 524-535, 2011.

[9] A.A. Alonge and T.J. Afullo: "Regime analysis of rainfall drop-size distribution models for microwave terrestrial networks," *IET Microwave, Antennas and Propagat*., Vol. 6, No. 4, March 2012.

[10] ITU-R P.837-1 Recommendation, "Characteristics of precipitation for propagation modelling," Geneva, 1994.

[11] P.O. Akuon and T.J.O. Afullo: "Rain cell sizing for the design of high capacity radio link systems in South Africa," *Progress in Electromagnetics Research B*, Vol. 35, pp. 263-285, 2011.

[12] T.J.O. Afullo: "Raindrop size distribution modelling for radio link design along the eastern coast of South Africa," *Progress In Electromagnetics Research B*, Vol. 34, pp. 345-366, 2011.

[13] ITU-R P.837-4 Recommendation: "Characteristics of precipitation for propagation modelling," Geneva, 2003.

[14] R.K. Crane: *Electromagnetic Wave Propagation through Rain*, Wiley Interscience, New York, 1996.

[15] R.L. Olsen, D.V. Rogers, and D.B. Hodge: "The aR^b relation in the calculation of rain attenuation," *IEEE Trans. Antennas Propagat*., vol. AP-26, pp. 318-329, March. 1978.

[16] ITU-R P.838-3 Recommendation: "Specific attenuation model for use in prediction methods," Geneva, 2005.

[17] M.O. Fashuyi and T.J. Afullo: "Rain attenuation and modelling for line-of-sight links on terrestrial paths in South Africa," *Radio Science*, Vol. 42, RS5006, doi:10.1029/2007RS003618, 2007 pp. 1-15.

[18] J. Wang, B.L. Fisher and D.B. Wolff: "Estimating rain rates from tipping-bucket rain measurements," *Journal of Atmospheric and Oceanic Technology*, pp. 1-45, 2006.

[19] Distromet system: *The Joss-Waldvogel Disdrometer Handbook*, Basel, Switzerland, 2000.

[20] M.J. Bartholomew: "Disdrometer and tipping bucket raingauge handbook," DOE/SC-ARM/TR-079, *ARM Climate Research Facility*, December 2009.

[21] F. Moupfouma: "More about rainfall rates and their prediction for radio systems," *IEEE Proceedings*, Vol. 134 (6), Pt. H, 527-537, 1987.

[22] E. Matricciani: "A mathematical theory of de-integrating long-time integrated rainfall and its application for predicting 1-min rain rate statistics," *International Journal of Satellite Communications and Networking*, 29:501-530, 2011.

[23] B. Segal: "The influence of the raingauge integration time on measured rainfall-intensity distribution functions", *Journal of Atmospheric and Oceanic Technology*, Vol.3, pp. 662-671, December 1986.

[24] C.W. Ooi and J.S. Mandeep: "Empirical methods for converting rainfall rate distribution from several higher integration times into a one-minute integration time in Malaysia," *GEOZIFIKA*, Vol. 30, pp. 143-154, November 2013.

[25] R.K. Flavin: "Rain attenuation considerations for satellite paths," *Telecom Australia Research Laboratories Report*, No. 7505, 1982.

[26] M. Galoie, G. Zenz and A. Motamedi: "Rainfall analysis for the Schoeckelbach Basin (Australia) and determining its best-fit probability distribution model," DOI:10.5675/ICWRER_2013, pp. 43-52.

[27] F. Moupfouma and S. Martin: "Modeling of the rainfall rate cumulative distribution for design of satellite and terrestrial communication systems," *International Journal of Satellite Communication*, Vol. 13, No. 2, pp. 105-115, 1995.

[28] P.L. Rice and N.R. Holmberg: "Cumulative Time Statistics of Surface-Point Rainfall Rates," *IEEE Transactions on Communications*, Vol. COM-21, No. 10, pp. 1131-1136, 1973.

[29] F. Rubel and M. Kottek, "Observed and Projected Climate Shifts 1901-2100 Depicted by World Maps of the Köppen-Geiger Classification," *Meteorologische Zeitschrift*, Vol. 10, No. 2, pp. 135-141, 2010.

[30] D.C.U Conradie: "South Africa's Climatic Zones: Today, Tomorrow," *International Green Building Conference and Exhibition*, Sandton, South Africa, July 2012.

[31] P.A. Watson, M. Gunes: B.A. Potter, V. Sathiaseelan, and J. Leitao, "Development of a climatic map of rainfall attenuation for Europe," Final Report of *ESA/ESTEC* Contract No. 4162/79/NL/DG/(SC), Report 327, 1982.

[32] ITU-R P.837-5 Recommendation: "Characteristics of Precipitation for Propagation Modelling," Geneva, 1994.

[33] ITU-R P.837-6 Recommendation: "Characteristics of Precipitation for Propagation Modelling," Geneva, 2012

[34] N. Guo, R.C. Qui, S.S. Mo and K. Takahashi: "60-GHz Millimeter-Wave Radio: Principle, technology and new results," Research Article, *EURASIP Journal on Wireless Communications and Networking*, Volume 2007, pp. 1-8, December, 2004.

LOG-DOMAIN ITERATIVE SPHERE DECODER WITH SYMBOL SORTING

P.R. Botha* **and B.T. Maharaj†**

* *Dept. of Electrical, Electronic & Computer Engineering, Corner of University Road and Lynnwood Road, University of Pretoria, Pretoria 0002, South Africa E-mail: prbotha@ieee.org*

† *Faculty of Engineering, Built environment and IT, Corner of University Road and Lynnwood Road, University of Pretoria, Pretoria 0002, South Africa E-mail: ssinha@saiee.org.za E-mail: sunil.maharaj@up.ac.za*

Abstract: In this paper the authors propose modified branch and pruning metrics for the sphere decoder to facilitate the use of apriori information in the sphere decoder. The proposed sphere decoder operates completely in the log-domain. Additionally the effect of order in which the symbols are decoded on the computational requirements of the decoder are investigated with the authors proposing a modification of the sorted QR decomposition (SQRD) algorithm to incorporate apriori information. The modified SQRD algorithm is shown to reduce the average number of computations by up to 95%. The apriori sphere decoder is tested in an iterative multiple input multiple output (MIMO) decoder and shown to reduce the bit error rate (BER) by an order of magnitude or provide approximately a one decibel improvement.

Key words: Sphere decoder, iterative decoding, MIMO, TAST, QR.

1. INTRODUCTION

The ever increasing demand for affordable, high speed and reliable wireless communication has led to the development of various technologies such as multiple input multiple output (MIMO) systems. The usage of multiple transmit and receive antennas of a MIMO system can potentially result in a significant increase in the capacity of the communication channel. Using MIMO in tandem with other communication techniques, such as orthogonal frequency division multiplexing (OFDM), enables the transmission of information over time, space and frequency.

The performance of a wireless communication system can also be greatly increased by exploiting some or all of the diversity, independently faded signal paths, in the wireless channel. Various coding schemes that aide in the utilisation of all of the available diversity and/or capacity in a MIMO channel have been proposed [1–4]. These codes generally require *joint* decoding using methods such as the Zero-Forcing (ZF), Minimum Mean Squared Error (MMSE) and Sphere decoder (SD) [5, 6]. Forward Error Correction FEC is also typically used to improve the performance of the system. Accurate soft outputs from the decoder can typically provide a 2dB gain [7] and is therefore desired. In this paper Max-log-map Hard-to-Soft decoding is used [8].

Drawing on the concept of turbo-codes [9], iteratively decoding can also provide an increase in performance. This entails a MIMO decoder that can use soft-inputs generally as apriori information. In [10] the authors provide a means to incorporate apriori information in the ZF and MMSE decoder. An alternative method that can be used to implement a soft-input sphere decoder [8] is also described and shown to be limited to BPSK and QPSK signal constellations. A similar approach is used by the authors of [11] without addressing nor identifying the limitations of their approach.

In this paper the authors will describe a modification to the branch and pruning metrics of the sphere decoder of [6] that incorporates apriori information. Studer et al in [12] propose what seems to be a similar approach to the approach used in this paper. They, however, focus on optimizing the MAP values whereas in this paper the focus is on the complexity introduced by the delayed pruning due to apriori information. It will be shown empirically that for iterative decoding the modification typically results, contrary to what is expected, in a reduction in the computations required by the sphere decoder is achieved.

Additionally, the effects of various symbol sorting strategies on the computational complexity of the apriori sphere decoder will be shown. It will be shown that a modified instance of the sorted QR decomposition (SQRD) [13] yields the greatest reduction in computations.

Notation: In this paper we use the following notation. Vectors are denoted by boldface lowercase letters. Matrices are denoted by boldface uppercase letters. Superscripts $\mathcal{T}$ and $\mathcal{H}$ denote the transpose and Hermitian transpose operations, respectively; $diag(d_1 \dots d_N)$ denotes a $N \times N$ diagonal matrix with diagonal entries $d_1 \dots d_N$. $\mathbf{F_N}$ is the $N \times N$ discrete Fourier transform (DFT) matrix and $(\cdot)$ denotes the dot product of two vectors.

2. MAP MIMO DECODING

The received signal in a MIMO system may be described as:

$$\mathbf{y} = \mathbf{H}\mathbf{x} + \mathbf{n}, \tag{1}$$

where $\mathbf{H}$ is the equivalent channel matrix, $\mathbf{x}$ is the transmitted data vector and $\mathbf{n}$ is the noise vector. In general $\mathbf{H}$, $\mathbf{x}$, $\mathbf{y}$ and $\mathbf{n}$ are complex valued. The optimal decoding of the receive signal involves the MAP calculation of the value of a bit. This probability is generally expressed in terms of log likelihood ratios (LLR) defined as:

$$\lambda_i = \ln\left(\frac{P(b_i=+1)}{P(b_i=-1)}\right), \tag{2}$$

where λ is the LLR and $P(b_i = x)$ is the probability that $b_i = x$. BPSK signalling has been assumed for the individual bit values instead of 0 and 1.

Using equation 2 and Bayes' rule, the MAP solution can be given as:

$$\tilde{\mathbf{x}} = \arg\min_{\mathbf{x}\in\mathbb{X}} \ln\{P(\mathbf{y}|\mathbf{x},\mathbf{H})\mathbf{P}(\mathbf{x})\}, \tag{3}$$

where the conditional probability $P(\mathbf{y}|\mathbf{x},\mathbf{H})$ is given by:

$$P(\mathbf{y}|\mathbf{x},\mathbf{H}) = \frac{1}{\pi^{N_R}\det(\Sigma)}\cdot \exp\left[-(\mathbf{y}-\mathbf{H}\mathbf{x})^{\mathcal{H}}\Sigma^{-1}(\mathbf{y}-\mathbf{H}\mathbf{x})\right], \tag{4}$$

where N_R is the number of receive antennas and Σ denotes the covariance matrix of $(\mathbf{y}-\mathbf{H}\mathbf{x})$ given by:

$$\Sigma = E\left[(\mathbf{y}-\mathbf{H}\mathbf{x})(\mathbf{y}-\mathbf{H}\mathbf{x})^{\mathcal{H}}\right]. \tag{5}$$

Since the noise $\mathbf{n}$ is assumed to be AWGN the following simplification may be made:

$$\Sigma = \sigma_n^2\mathbf{I}_{\mathbf{N_R}}, \tag{6}$$

$$\det(\Sigma) = \sigma_n^{2N_R}, \tag{7}$$

$$\Sigma^{-1} = \frac{1}{\sigma_n^2}, \tag{8}$$

where σ_n^2 is the noise power and I_k is the $k\times k$ identity matrix. Using equations 2 to 8 the MAP solution can be expressed as:

$$\lambda_i^p \approx \min_{\mathbf{x}\in\mathbb{X}_{\exists}^{\exists-\nu}}\left\{\frac{||\mathbf{y}-\mathbf{H}\mathbf{x}||^2}{\sigma_n^2} - \frac{1}{2}\mathbf{b}\cdot\lambda^{\mathbf{a}}\right\} - \min_{\mathbf{x}\in\mathbb{X}_{\exists}^{\exists+\nu}}\left\{\frac{||\mathbf{y}-\mathbf{H}\mathbf{x}||^2}{\sigma_n^2} - \frac{1}{2}\mathbf{b}\cdot\lambda^{\mathbf{a}}\right\}, \tag{9}$$

where λ_i^p is the LLR of the MAP of the i^{th} bit, b_i, with $\mathbb{X}_{\exists}^{\exists\curvearrowleft}$ denoting the set of all transmit vectors having $b_i = x$. $\mathbf{b}$ denotes the vector of bits associated with $\mathbf{x}$ and λ^a is the vector of apriori LLRs. Additional use of the max-log approximation:

$$\ln\left(\sum_i e^{x_i}\right) \approx \max_i x_i, \tag{10}$$

was made in the derivation of equation 9.

Thus the decoding problem involves the calculation of the *most* likely metric for both possible values of the bit in question. Non-iterative decoders typically assume that there is no apriori information.

3. CLASSICAL SPHERE

The sphere decoder in [6] is essentially a tree search algorithm. It is a variation of the A* tree search algorithm [14, 15]. In the classical sphere decoder the A* algorithm is used to solve the following system of linear equations:

$$\tilde{\mathbf{x}} = \arg\min_{\mathbf{x}\in\mathbb{X}}\left\{\frac{\|\mathbf{y}-\mathbf{H}\mathbf{x}\|^{\mathbf{2}})}{\sigma_n^2}\right\}, \tag{11}$$

in order to obtain the MAP transmitted channel symbols and, thus, transmitted data. This is essentially the same as equation 9 without the apriori information. For use with the sphere decoder, equation 11 is transformed into a triangular system. In [6], as with most other formulations, the Cholesky decomposition:

$$\mathbf{R}^{\mathcal{H}}\mathbf{R} = \mathbf{A}, \tag{12}$$

where $\mathbf{R}$ is upper triangular, is used. Equation 11 is then transformed into the triangular equation:

$$\tilde{\mathbf{x}} = \arg\min_{\mathbf{x}\in\mathbb{X}}\left\{(\mathbf{x}-\hat{\mathbf{x}})^{\mathcal{H}}\mathbf{R}^{\mathcal{H}}\mathbf{R}(\mathbf{x}-\hat{\mathbf{x}})\right\}, \tag{13}$$

where $\hat{\mathbf{x}}$ is the zero-forcing solution, and $\mathbf{R}^{\mathcal{H}}\mathbf{R} = \mathbf{H}^{\mathcal{H}}\mathbf{H}$ and σ_n^2 has been omitted as it is a constant and does not affect the result. The zero-forcing solution, $\hat{\mathbf{x}}$ can be obtained using, for example, the Moore-Penrose Pseudo inverse:

$$\mathbf{A}^{\dagger} = (\mathbf{A}^{\mathcal{H}}\mathbf{A})^{-\mathbf{1}}\mathbf{A}^{\mathcal{H}}, \tag{14}$$

as:

$$\hat{\mathbf{x}} = \mathbf{H}^{\dagger}\mathbf{y}. \tag{15}$$

Alternatively the QR decomposition, SV decomposition, LU decomposition or even the Cholesky decomposition can be used to compute the zero-forcing solution. Equation 11 can also be transformed into a triangular system using the QR decomposition:

$$\tilde{\mathbf{x}} = \arg\min_{\mathbf{x}\in\mathbb{X}}\left\{\|\mathbf{Q}^{\mathcal{H}}\mathbf{y}-\mathbf{R}\mathbf{x}\|^{\mathbf{2}}\right\}, \tag{16}$$

where $\mathbf{QR} = \mathbf{H}$. This formulation will be used henceforth.

The tree structure arrises from the observation that $x \in \mathbf{X}$, i.e. the channel symbol x is part of a finite set $\mathbf{X}$ and that when performing the back substitution, the value of the current symbol is dependent on the previous symbols.

In equations 13 & 16 it is important to note that when the equations are being evaluated, the evaluations can be calculated by traversing the tree on a *symbol-by-symbol* basis and are *monotonously* increasing:

$$T_{n-1} \geq T_n, \tag{17}$$

where it should be noted that the tree is traversed from node N upwards in an upper triangular system. Thus, as soon as the metric for a branch, T_n in the tree exceeds the current lowest metric, $T_{\min}$, it will *always* exceed that metric and therefore the branch can be pruned from the solution space. In such cases, the A* algorithm is the optimal tree-traversal algorithm [14]. In the next section it will be shown that should apriori information be incorporated into the MAP solution, then the branch metric is no longer monotonously increasing. Thus, a branch can no longer be pruned from the tree once its metric exceeds the current minimum.

4. APRIORI SPHERE DECODER

The MAP solution including apriori information is given by:

$$\tilde{\mathbf{x}} = \arg\min_{\mathbf{x}\in\mathbb{X}} \left\{ \frac{\|\mathbf{y}-\mathbf{H}\mathbf{x}\|^2}{\sigma_n^2} - \frac{\boldsymbol{\lambda}\cdot\mathbf{b}}{2} \right\}, \tag{18}$$

where $\boldsymbol{\lambda}$ is the Log-Likelihood Ratio of the apriori information and $\mathbf{b}$ is the bitwise data vector, in BPSK, representation of $\mathbf{x}$.

Equation 18 can be partly transformed into a triangular system as in section 3.:

$$\tilde{\mathbf{x}} = \arg\min_{\mathbf{x}\in\mathbb{X}} \left\{ \frac{\|\mathbf{Q}^{\mathcal{H}}\mathbf{y}-\mathbf{R}\mathbf{x}\|^2}{\sigma_n^2} - \frac{\boldsymbol{\lambda}\cdot\mathbf{b}}{2} \right\}, \tag{19}$$

where it should be noted that σ_n^2 can no longer be omitted from the calculations. Whilst eq. 19 can still be represented as a tree structure, it is evident that the equation is no longer monotonously increasing. In the event that the current branch metric, T_n exceeds the minimum metric, $T_{\min}$ it is still possible that the remaining apriori information can result in the branch metric being lower than the current minimum.

Therefore it is no longer possible to prune the branch the moment the branch metric exceeds the current minimum metric as was the case with the classical sphere decoder. It should be mentioned that for BPSK and QPSK channel symbols it is possible to incorporate the apriori information vector, $\boldsymbol{\lambda}$, into the received vector, $\mathbf{y}$ [8]. This approach does not work for other modulation constellations [10].

It is therefore necessary to modify the pruning metric to incorporate the apriori information in $\boldsymbol{\lambda}$. The pruning metric now only prunes a branch, if the current branch metric exceeds the current minimum *and* the remaining apriori information is insufficient to change this. Thus the branch is pruned when:

$$T_n - \frac{1}{2}\sum_{i=n}^{N} \lambda_i > T_{\min}, \tag{20}$$

where λ_i is the apriori information associated with the channel symbol x_i. Whilst the new pruning metric allows the sphere decoder to incorporate the apriori information, it potentially delays the pruning of branches potentially increasing the average number of computations. However, it is possible to re-arrange the tree such that the branches are pruned earlier as is discussed in the next section.

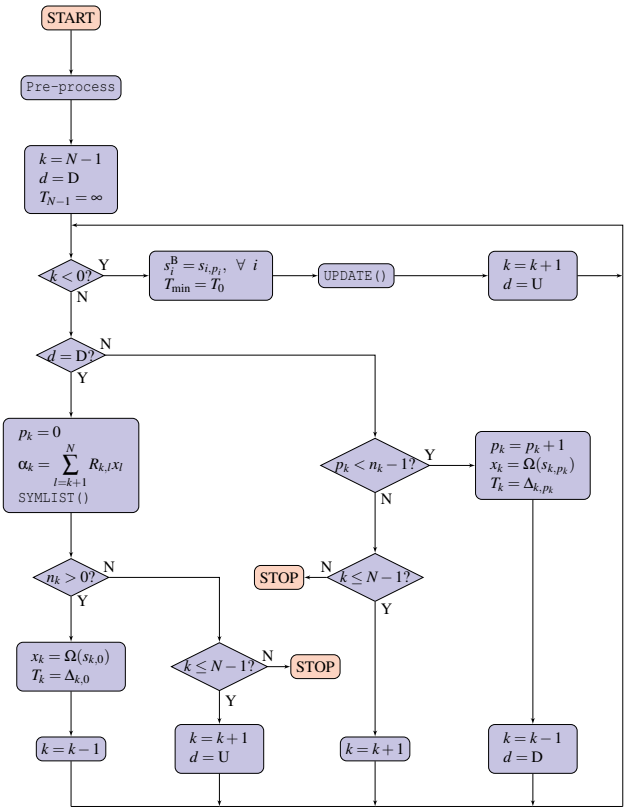

Figure 1: Flow diagram of the tree search algorithm.

5. RE-ORDERING OF SYMBOLS

In order to prune branches on the tree, it is known that having the diagonal of $\mathbf{R}$ be ordered *ascendantly*, i.e. $|r_{n+1,n+1}| \geq |r_{n,n}|$ can speed up the sphere decoder [16]. Similarly the apriori sphere decoder can be sped up by ordering the symbols. Two approaches have been investigated: one based solely on the apriori information $\boldsymbol{\lambda}$, the other based on apriori information *and* the channel $\mathbf{H}$.

5.1 *Re-ordering by* $\boldsymbol{\lambda}$

The reasoning behind ordering the tree based on the apriori information is the idea of reducing the impact of the remaining apriori information on the classical pruning metric. Thus, ideally the tree should be traversed in the *descending* order of λ_n, where λ_n is:

$$\lambda_n = \sum_{i=0}^{N_b-1} |\lambda_i|, \tag{21}$$

i.e. the sum of the absolute values of the LLRs of the bits of symbol n. In this manner the sum of absolute values of the LLRs diminishes rapidly as the tree is traversed by the decoder. Since the system being decoded has been transformed into an upper triangular system, this means

that the channel symbols and their respective columns in $\mathbf{H}$ must be sorted based on the *ascending* values of λ_n. λ_n is the total apriori information for symbol x_n given by the summation of the absolute values of the LLRs of each bit in symbol x_n.

5.2 Re-ordering by λ and $\mathbf{H}$

It is known that performing the triangular transformation in such a way that the diagonal elements, of the upper triangular system, are increasing results in a speedup of the sphere decoder [16]. A sub-optimal approximation is to sort the column of $\mathbf{H}$ according to their Frobenius norms.

In an attempt to combine the ordering of the symbols with the norms of the columns of $\mathbf{H}$ with their ordering with respect to their apriori information, the following metric, inspired by eq. 19, is proposed:

$$C_n = \frac{1}{\sigma_n^2} \sum_{i=0}^{N_{RX}-1} |H_{i,n}|^2 + \frac{1}{2}\lambda_n. \tag{22}$$

The symbols are then ordered ascendantly according C_n. Equation 22 scales the contribution of the channel by the noise power. The first term is essentially an indicator of the SNR of symbol n.

5.3 Sorted QR Decompostion

The sorted QR decompostion proposed in [13] attempts to order the diagonal elements of $\mathbf{R}$ in increasing orders of magnitude. The algorithm is:

$\mathbf{R} = \mathbf{0}$, $\mathbf{Q} = \mathbf{H}$ & $\mathbf{P} = \mathbf{I_{N_T}}$
for $n = 0$ to $N_T - 1$ **do**
  $k_n = \underset{j=n,\cdots,N_T}{\arg\min} |\mathbf{q_j}|^2$
  exchange columns n and k_n in $\mathbf{Q}$, $\mathbf{R}$ and $\mathbf{P}$
  $R_{n,n} = |\mathbf{q_n}|$
  $\mathbf{q_n} = \mathbf{q_n}/\mathbf{R_{n,n}}$
  for $j = n+1$, to $N_T - 1$ **do**
    $R_{n,j} = \mathbf{q_n^{\mathcal{H}}}\mathbf{q_j}$
    $\mathbf{q_j} = \mathbf{q_j} - \mathbf{R_{n,j}}\mathbf{q_n}$
  end for
end for

where $\mathbf{q_n}$ is the n^{th} column of matrix $\mathbf{Q}$. $\mathbf{P}$ is the permutation matrix by which the columns of $\mathbf{H}$ and the rows of $\mathbf{x}$ have been permuted.

5.4 Modified Sorted QR Decomposition

The standard SQRD does not make use of information other than the channel matrix $\mathbf{H}$. The authors therefore propose the following modified SQRD (mSQRD)algorithm:

$\mathbf{R} = \mathbf{0}$, $\mathbf{Q} = \mathbf{H}$ & $\mathbf{P} = \mathbf{I_{N_T}}$
for $n = 0$ to $N_T - 1$ **do**
  $\lambda_k^s = \sum_{k=0}^{N_b} |\lambda_{nN_b+k}|$
end for
for $n = 0$ to $N_T - 1$ **do**
  $k_n = \underset{j=n,\cdots,N_T}{\arg\min} \left\{ \frac{\|\mathbf{q_j}\|^2}{\sigma_n^2} + \frac{1}{2}\lambda_j^s \right\}$
  exchange columns n and k_n in $\mathbf{Q}$, $\mathbf{R}$, $\mathbf{P}$ and λ^s
  $R_{n,n} = |\mathbf{q_n}|$
  $\mathbf{q_n} = \mathbf{q_n}/\mathbf{R_{n,n}}$
  for $j = n+1$, to $N_T - 1$ **do**
    $R_{n,j} = \mathbf{q_n^{\mathcal{H}}}\mathbf{q_j}$
    $\mathbf{q_j} = \mathbf{q_j} - \mathbf{R_{n,j}}\mathbf{q_n}$
  end for
end for

where σ_n^2 is the noise variance and N_b is the number of bits per symbol.

6. ALGORITHM DETAILS

The apriori sphere decoder is based on the implementation by [6]. It has been modified to use the QR decomposition instead of the Cholesky decomposition. The flow diagram for the apriori sphere decoder is shown in figure 1.

6.1 Pre-processing

The `Pre-process` block is responsible for calculating the best symbol order to obtain the permutation matrix $\mathbf{P}$, the QR decomposition of $\mathbf{H}$ as well as the calculation of the cumulative LLRs λ^c:

for $i = 0$, to $N - 1$ **do**
  $\lambda_i^c = \lambda_{i-1}^c + \sum_{j=0}^{N_b-1} |\lambda_{i \cdot N_b + j}|$
end for
$\mathbf{P} \leftarrow$ Optimal symbol order for decoding
$\mathbf{Q}, \mathbf{R} \leftarrow \mathrm{qr}(\mathbf{HP^{-1}})$
$\mathbf{y} \leftarrow \mathbf{Q^{\mathcal{H}}}\mathbf{y}$

where $\lambda_{-1} = 0$.

6.2 Symlist

The `SYMLIST()` function calculates the possible symbols for the level and calculates their metrics. The symbols are then sorted ascendantly according to the metric. The variable n_k is then assigned the number of symbols that are smaller than the pruning metric:

for $i = 0$, to $Ns - 1$ **do**
  $\beta_i = \sum_{j=0}^{N_b-1} \lambda_{j+N_b k} \hat{b}_j^i$
  $\Delta_i^k = \frac{\|y_k - \alpha_k - R_{k,k}\Omega(i)\|^2}{\sigma_n^2} - \frac{1}{2}\beta_i + \Delta_{p_{k+1}}^{k+1}$
end for
`sort(`Δ^k, s^k`)`
$n_k = \underset{i}{\arg\max} \left\{ \Delta_i^k < T_{\min} + \frac{1}{2}\lambda_k^c \right\}$
$T_k = \Delta_0^k$

where $\hat{b}_j^i$ denotes the j^{th} bit represented by symbol i. The `sort()` function sort the symbols ascendantly according to their Δ_i^k metrics and stores the symbol order in s_i^k. The

number of symbols that are less than the pruning metric is stored in n_k.

Performance metric: The `SYMLIST()` function is the function where the vast majority of the calculations are performed. It is also visited for each node in the tree. Thus, the number of times the `SYMLIST()` function is called is used as a performance metric in evaluating the relative performance of the sphere decoder with regard to various symbol ordering strategies. This allows the metric to be independent of the specific implementation architecture and programming.

6.3 Update

The `UPDATE()` function uses the newly found minimum metric T_{min} to prune the tree. ItiIterates through the levels and updates the n^k value for each level by only keeping the symbols whose metrics are less than the new pruning metric:

for $k = 0$, to $N-1$ **do**

$$n^k = \arg\max_j \left\{ \Delta_j^k < T_{\min} + \frac{1}{2}\lambda_k^c \right\}$$

end for

7. SYSTEM DESCRIPTION

The iterative decoding of linear pre-coded (LP) MIMO will be used to test the performance of the apriori sphere decoder. A short LDPC code is used to provide the apriori information to the MIMO decoder from the second iteration onwards.

7.1 Linear Pre-coding

Linear pre-coding of a MIMO system using threaded algebraic space time (TAST) codes enables the exploitation of all of the diversity in a MIMO channel without sacrificing transmission rate [2]. This is achieved by linearly mapping the channel symbol vector to a new encoded channel symbol vector. The linearity of the mapping enables the mapping to be expressed as a matrix multiply. Let $\mathbf{x} = [\mathbf{x_1}, \cdots \mathbf{x_m}]^{\mathcal{T}}$ be a data vector of length N complex channel symbols taken from a modulation alphabet $\mathbf{X}$ such as QPSK or M-QAM. Let Θ be a unitary matrix of dimensions $N \times N$ defined as [2]:

$$\Theta = \mathbf{F_N^{\mathcal{H}}} \mathrm{diag}(\mathbf{1}, \varphi, \ldots, \varphi^{\mathbf{N-1}}), \tag{23}$$

where $\varphi = \exp(\mathrm{j}2\pi/4N)$ and $\mathbf{F_N}$ is the $N \times N$ discrete Fourier transform matrix. The mapping operation can thus be expressed as:

$$\mathbf{s} = \Theta \mathbf{x}, \tag{24}$$

where $\mathbf{s}$ is the newly encoded channel symbol vector. In a noiseless environment the correct decoding of the entire $\mathbf{x}$ channel symbol vector only requires the correct reception of a single encoded symbol of $\mathbf{s}$ achieving diversity equal to the rank of Θ, R_Θ. Two or more streams of LP encoded vectors can be layered together in order to exploit the full rate of the channel. Diophantine numbers aide the decoder in separating the various streams from each other [2]. The Diophantine number for each layer is obtained by : $\phi_n = \varphi^n, \;\; n = 0, \ldots, N_L - 1$, where N_L is the number of layers.

The disadvantage of TAST codes is their decoding complexity as $N_L \times N$ symbols need to be *jointly* decoded.

7.2 MIMO System

In this paper the MIMO channel is modelled as an $N_R \times N_T$ matrix, $\mathbf{H}$. The elements of $\mathbf{H}$ are each i.i.d. complex Gaussian with zero mean and unit variance. This corresponds to an ideal Rayleigh fading channel with no correlation. Time and frequency diversity can be expressed as a matrix with MIMO channel blocks on the diagonal. In this paper it is also assumed that time and frequency are independently faded. The full system equation then becomes:

$$\mathbf{y} = \mathbf{H}'\Theta'\mathbf{P}\mathbf{x}' + \mathbf{n}, \tag{25}$$

with $\mathbf{P}$ a permutation matrix that determines the manner in which the two streams are threaded together.

With layering, the matrices $\mathbf{H}', \Theta'$ and $\mathbf{x}'$ are given as:

$$\mathbf{H}' = \begin{bmatrix} \mathbf{H_0} & \mathbf{0} & \mathbf{0} & \mathbf{0} \\ \mathbf{0} & \mathbf{H_1} & \mathbf{0} & \mathbf{0} \\ & & \ddots & \\ \mathbf{0} & \mathbf{0} & \ddots & \mathbf{0} \\ \mathbf{0} & \mathbf{0} & \mathbf{0} & \mathbf{H_{N_H-1}} \end{bmatrix}, \tag{26}$$

$$\Theta' = \begin{bmatrix} \Theta\varphi^0 & \mathbf{0} & \mathbf{0} & \mathbf{0} \\ \mathbf{0} & \Theta\varphi^1 & \mathbf{0} & \mathbf{0} \\ & & \ddots & \\ \mathbf{0} & \mathbf{0} & \ddots & \mathbf{0} \\ \mathbf{0} & \mathbf{0} & \mathbf{0} & \Theta\varphi^{N_L-1} \end{bmatrix}, \tag{27}$$

$$\mathbf{x}' = \begin{bmatrix} \mathbf{x_0^{\mathcal{T}}} & \mathbf{x_1^{\mathcal{T}}} & \cdots & \mathbf{x_{N_L-1}^{\mathcal{T}}} \end{bmatrix}^{\mathcal{T}}, \tag{28}$$

where N_H is the number of individual MIMO transmissions that are made, either in frequency or time, and is given by $N_L \times R_\Theta / N_T$. The simulations in this paper are made with $R_\Theta = 4$, $N_T = N_R = N_L = 2$ and with a resultant $H_N = 4$.

7.3 Turbo Structure

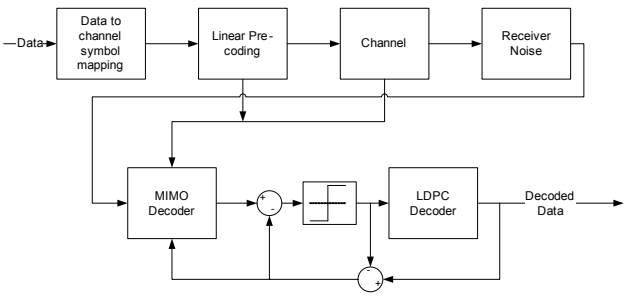

Figure 2: Block diagram of the iterative decoder system.

Figure 2 shows the block diagram of the iterative turbo MIMO decoder. The binary data is mapped to uncoded channel symbols which are then mapped to and layered to LP encoded channel symbols. These encoded channel symbols are transmitted over the Rayleigh faded MIMO channel. At the receiver the channel symbols are received and AWGN is added. The MIMO decoder uses the information about the LP code, Θ', the channel information $\mathbf{H}'$ and the signal constellation to soft decode the data into MAP LLR values.

In the initial iteration there is no extrinsic information provided by the FEC code. Thus the initial input to the FEC decoder is the aposteriori output of the MIMO decoder. On subsequent iterations the intrinsic information is subtracted from the aposteriori information from the FEC decoder to yield the extrinsic information from the FEC decoder which is used by the MIMO decoder as apriori information. Similarly the input to the FEC decoder, on subsequent iterations, is obtained by subtracting the intrinsic information from the aposteriori information of the MIMO decoder.

Hard Limiting of the LLRs: It was found that it was necessary to limit the magnitude of the LLRs provided to the LDPC decoder especially specifically at high SNR values, for performance and stability reasons. In the event that the LLRs were too large, the specific LDPC used decoder would breakdown. Hard limiting of the magnitude of the LLRs was done on the input to the LDPC decoder. The effect of the value of the hard limit threshold on the BER of the system is shown in figures 3 & 4. It is shown that at the specific E_b/N_0 values in the figure that a low threshold of around five (5) is optimal. The two figures also show the diminishing returns that each additional iteration provides.

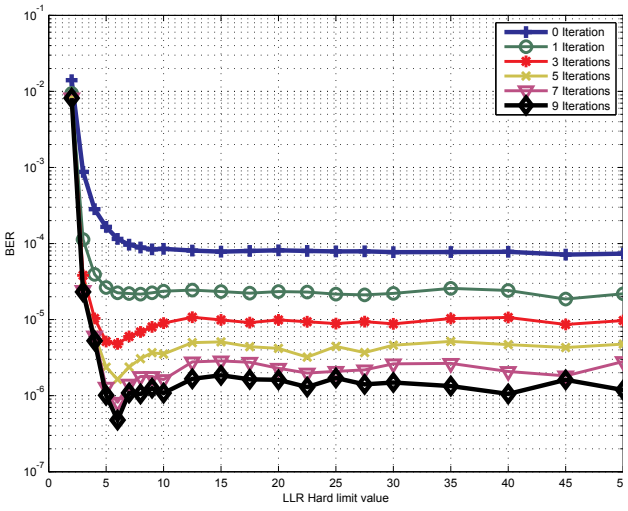

Figure 3: Effect of LLR hard limiting threshold on the BER for QPSK at 11dB E_b/N_0.

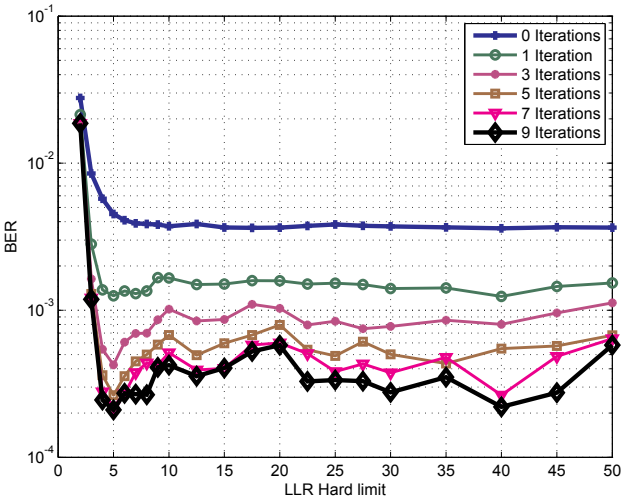

Figure 4: Effect of LLR hard limiting threshold on the BER for 16QAM at 15dB E_b/N_0.

8. RESULTS

Figure 5 shows the effects iterative decoding has on the BER performance of the MIMO system for case of a QPSK signal constellation and a 16QAM signal constellation. It is evident that the BER is reduced by an order of magnitude for both constellations. Due to the steep slope of the BER curve, this only corresponds to a 1 dB improvement as measured at 10^{-4}.

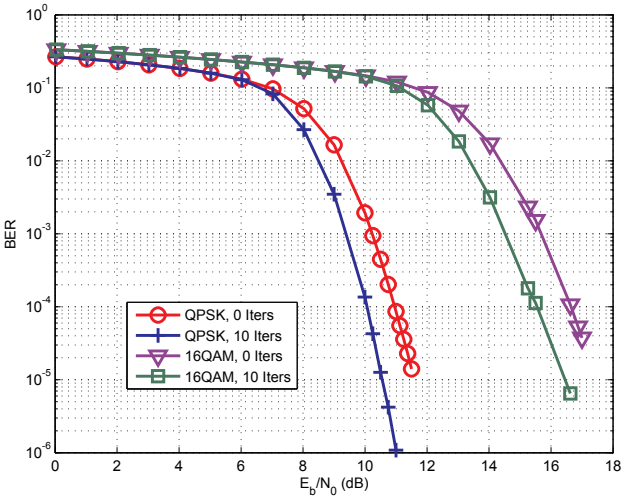

Figure 5: Plot of the BER for QPSK and 16QAM showing the effects of ten decoding iterations on the BER.

The decrease in the number of `SYMLIST()` calls made by the decoder for QPSK and 16QAM signal constellations are shown in figures 6 & 7 respectively. The decrease in the number of function calls is with respect to the unsorted decoder. It is seen in figure 6 that the mSQRD and SQRD perform similarly in the low E_b/N_0 regions, followed by the sub-optimal $\mathbf{H}+\lambda$ ordering method. At higher E_b/N_0 values the mSQRD and $\mathbf{H}+\lambda$ start outperforming the SQRD algorithm. With the mSQRD algorithm a maximum

speed up of 42.5% is achieved for QPSK.

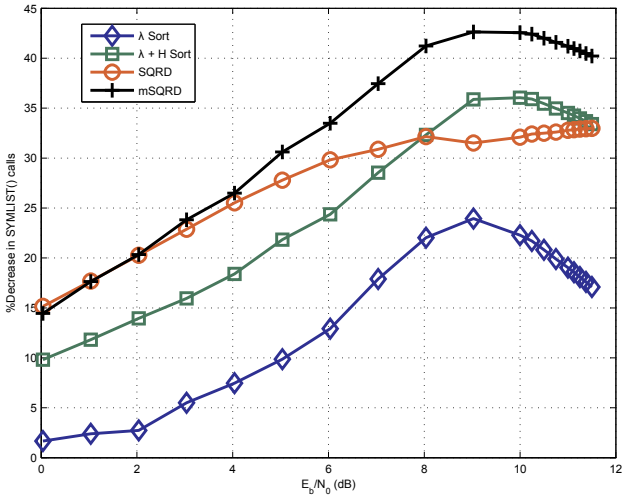

Figure 6: Plot in of the decrease in SYMLIST() calls for each of the sorting methods as compared to the unsorted case. QPSK.

Figure 7 shows that a significant performance increase is obtained from the SQRD based algorithms of approximately 35% at 0dB E_b/N_0 increasing to a maximum of approximately 70%. All of the methods incorporating channel information appear to perform similarly at higher E_b/N_0 values.

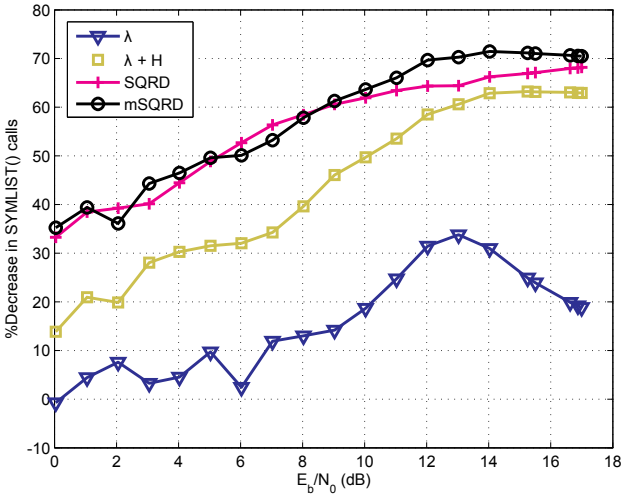

Figure 7: Plot in of the decrease in SYMLIST() calls for each of the sorting methods as compared to the unsorted case. 16QAM.

From figure 8 it can be noted that there is a distinct region where the addition of the apriori information adds to the decoding complexity; however, sorting based on λ does not appear to increase the complexity of subsequent iterations. The added complexity at low E_b/N_0 values is negligeable. At high E_b/N_0 the addition of apriori information substantially reduces the decoding complexity by up to 95%.

In figure 9 the average number of SYMLIST() calls per bit needed to perform hard output decoding is plotted for the

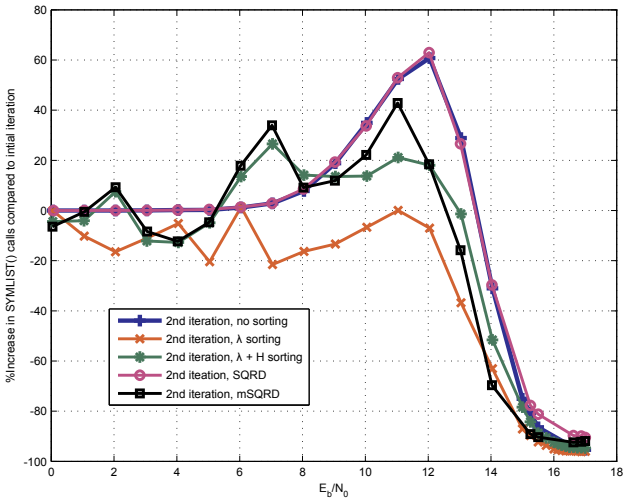

Figure 8: Plot of the increase in SYMLIST() calls due to the apriori pruning metric used in subsequent iterations vs. the normal sphere metric of the first iteration for the various sorting strategies. 16QAM.

unsorted sphere using the classical pruning metric. The figure show a decrease in the number of calls required as E_b/N_0 increases.

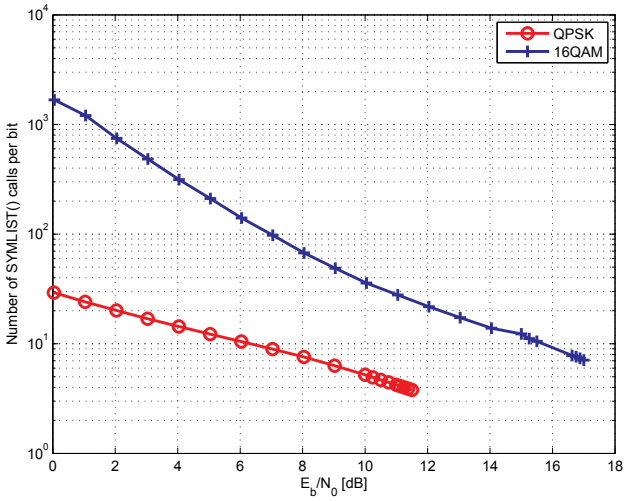

Figure 9: Plot of the number of SYMLIST() calls for the unsorted sphere decoder using the classic pruning metric for QPSK and 16QAM. Hard output decoding.

9. DISCUSSION

Whilst figures 6 & 7 show a definitive improvement at high E_b/N_0 values, it should also be kept in mind that the overall number of SYMLIST() calls at high E_b/N_0 is much less than at lower E_b/N_0 values. As such, it is ultimately expected that at *very* high E_b/N_0 values, the speed difference between the algorithms would converge to almost nothing. The sorting metrics incorporating channel information $\mathbf{H}$ yield an improvement of between 10% to 15% in the low E_b/N_0 regions for QPSK and between 15%

to 35% for 16QAM.

Considering that incorporating apriori information adds approximately, worst case, 60% additional calls, as compared to not using apriori information, but with the mSQRD also resulting in a 60% overall reduction in the number of calls the overall effect is that the apriori sphere decoder is not significantly more complex when used for iterative decoding. Deciding the decoding order based on λ does not appear to increase the decoding complexity at all. This is most likely due to the fact that the MAP outputs of both the MIMO decoder and the FEC decoder are supposed to, ideally, be highly correlated. Should that not be the case then the apriori decoder would likely have a significantly increased complexity.

Figure 9 shows that whilst the sorted algorithms yield a significant decrease in computations, with respect to the unsorted decoder, at high E_b/N_0 values, the decoding complexity is already an order of magnitude less for QPSK and two orders of magnitude for 16QAM.

10. CONCLUSION

In this paper an algorithm sphere decoder that accepts apriori information in LLR form was proposed. A simple iterative MIMO decoder was used to evaluate the algorithm practically. It was shown that sorting the order in which the symbols are decoded can have a great impact on the computational requirements of the algorithm. Based on the good performance of the SQRD algorithm in reducing the complexity of the decoder, a modification of the algorithm to incorporate apriori information was proposed. The mSQRD algorithm was shown to yield the greatest reduction in computational requirements of the decoder. It was also shown that in the case of iterative decoding the addition of apriori information does not significantly increase the computational requirements. The addition of apriori information actually reduced the computational requirements. This is contrary to what was expected since the pruning of the tree is delayed with the addition of apriori information.

REFERENCES

[1] S. Alamouti, "A simple transmit diversity technique for wireless communications," *IEEE Journal on Selected Areas in Communications*, vol. 16, no. 8, pp. 1451–1458, October 1998.

[2] H. El Gamal and M. Damen, "Universal space-time coding," *Information Theory, IEEE Transactions on*, vol. 49, no. 5, pp. 1097 – 1119, May 2003.

[3] V. Tarokh, H. Jafarkhani, and A. Calderbank, "Space-time block codes from orthogonal designs," *Information Theory, IEEE Transactions on*, vol. 45, no. 5, pp. 1456 –1467, July 1999.

[4] W. Zhang, X. G. Xia, and P. C. Ching, "High-Rate Full-Diversity Space-Time-Frequency Codes for Broadband MIMO Block-Fading Channels," *IEEE Transactions on Communications*, vol. 55, no. 1, pp. 25–34, 2007.

[5] J. Yoo, J. Lee, and P. Sin-Chong, "Performance evaluation of various MIMO decoders for IEEE 802.11n WLAN system," in *Communication Technology, 2006. ICCT '06. International Conference on*, November 2006, pp. 1 –3.

[6] Z. Safar, W. Su, and K. J. R. Liu, "A fast sphere decoding algorithm for space-frequency block codes," *EURASIP J. Appl. Signal Process.*, vol. 2006, pp. 148–148, January 2006. [Online]. Available: http://dx.doi.org/10.1155/ASP/2006/97676

[7] J. Proakis, *Digital communications*. Boston: McGraw-Hill, 2001.

[8] R. Wang and G. Giannakis, "Approaching MIMO channel capacity with soft detection based on hard sphere decoding," *IEEE Transactions on Communications*, vol. 54, no. 4, pp. 587–590, April 2006.

[9] C. Berrou and A. Glavieux, "Near optimum error correcting coding and decoding: turbo-codes," *Communications, IEEE Transactions on*, vol. 44, no. 10, pp. 1261 –1271, October 1996.

[10] P. Botha and B. Maharaj, "Turbo STFC decoding with the Zero Forcing decoder," in *AFRICON, 2011*, September 2011, pp. 1–5.

[11] T. Seifert, E. P. Adeva, and G. Fettweis, "Towards complexity-reduced soft-input soft-output sphere detection," in *Systems, Communication and Coding (SCC), Proceedings of 2013 9th International ITG Conference on*, January 2013, pp. 1–6.

[12] C. Studer and H. Bolcskei, "Soft-input soft-output single tree-search sphere decoding," *Information Theory, IEEE Transactions on*, vol. 56, no. 10, pp. 4827–4842, October 2010.

[13] D. Wubben, R. Bohnke, J. Rinas, V. Kuhn, and K. Kammeyer, "Efficient algorithm for decoding layered space-time codes," *Electronics Letters*, vol. 37, no. 22, pp. 1348–1350, October 2001.

[14] P. Hart, N. Nilsson, and B. Raphael, "A formal basis for the heuristic determination of minimum cost paths," *Systems Science and Cybernetics, IEEE Transactions on*, vol. 4, no. 2, pp. 100–107, July 1968.

[15] R. Dechter and J. Pearl, "Generalized best-first search strategies and the optimality of a*," *J. ACM*, vol. 32, no. 3, pp. 505–536, July 1985. [Online]. Available: http://doi.acm.org/10.1145/3828.3830

[16] C. Studer, A. Burg, and H. Bolcskei, "Soft-output sphere decoding: algorithms and vlsi implementation," *Selected Areas in Communications, IEEE Journal on*, vol. 26, no. 2, pp. 290 –300, February 2008.

EFFECT OF SURFACE DISCHARGES ON LIGHTNING IMPULSE BREAKDOWN VOLTAGE OF OIL-IMPREGNATED PRESSBOARD IN POWER TRANSFORMERS

M.M. Tshivhilinge and C. Nyamupangedengu

School of Electrical and Information Engineering, University of the Witwatersrand, Johannesburg, P. Bag, 3, Wits 2050, South Africa, E-mails: Mercy.Tshivhilinge@pttransformers.co.za; cuthbert.nyamupangedengu@wits.ac.za;

Abstract: Power transformers inevitably experience impulse over-voltage stresses such as from lightning and/or switching events despite various protection systems that may be in place. At locations along oil/pressboard interfaces in the transformer, surface discharges may initiate due to various reasons. The surface discharges may or may not eventually lead to voltage flashover faults. This paper presents a study of how relatively small surface discharges affect the lightning voltage impulse (LI) strength of oil-impregnated pressboard insulation. It is found that surface discharges of magnitudes in the order of some hundreds of pC can reduce the LI withstand voltage of the oil-impregnated pressboard by up to 15%. Although the negative polarity LI withstand voltage of surface discharge-aged pressboard is higher than that of positive polarity, the reduction in the LI voltage strength is more pronounced for the negative LI impulse voltage. The findings suggest further scrutiny of the standardised acceptable levels of PD in power transformers.

Keywords: Oil-impregnated pressboard, power transformers, surface discharges, lightning breakdown voltage

1. INTRODUCTION

Partial discharge (PD) is a phenomenon that is now widely acknowledged as both a symptom and agent of electrical insulation degradation [1]. In power transformers there are still some aspects of PD that are yet not well understood. As an example precise location of PD sources in power transformers is still a major challenge [2] although some successes have been reported in using the unconventional PD detection techniques such as ultra-high frequency (UHF) and acoustic methods [3-8].

A considerable body of knowledge of partial discharges in power transformers has been built up in the literature. However, PD location and knowledge of the minimum PD apparent charge magnitude above which the PD activity is considered dangerous still beg research attention. In power transformers PD measurements are commonly conducted in accordance with the IEC 60076-3 [9]. In the latest edition of the standard, IEC 60076-3 (2013) [10], the maximum acceptable PD magnitude has been reduced to 250 pC, while previously it was 500 pC. It is well known that the PD magnitude can be used to classify the defect causing PD in the transformer insulation system [1-3]. Surface discharges in power transformers are regarded as deleterious because once initiated they may progress to complete failure over time under normal operating voltage. The minimum magnitude of surface discharge that is deemed dangerous is still a subject of further research.

This paper presents results of an experimental study on how pre-exposure of oil-impregnated pressboard to surface discharges of an average magnitude below 500 pC affects the lightning impulse (LI) withstand voltage of the pressboard.

The next section gives a bird's eye view of the state of the art on how partial discharges affect the lightning withstand parameter of pressboard insulation. The experimental investigation is presented in section 3 which comprises of pressboard samples preparation, PD measurements, surface PD ageing procedure and the LI voltage withstand tests of the pressboard samples. The results are in section 4 and conclusion in section 5.

2. PD AND LI BREAKDOWN OF OIL-IMPREGNATED PRESSBOARD: A STATE OF THE ART REVIEW

Research work by Okabe et al, [11, 12], is a notable contribution to the knowledge on the relationship between PD and lightning impulse voltage breakdown of oil-impregnated pressboard. In [11], it is deduced that PD magnitude of at least 10 000 pC is harmful as it reduces the residual LI voltage withstand level of oil-impregnated pressboard insulation. The defect type studied comprised of a speck of a conducting solid material sandwiched between pressboard insulation.

The phenomenon of surface discharges on oil-impregnated pressboard has been extensively studied by many researchers with the objective of understanding the physical mechanisms [13-17]. A significant body of knowledge in that regard has been built up and a good state of the art review is in [13]. Surface discharges are understood to eventually lead to voltage flashover as they evolve through tracking (creepage) across the surface of the solid insulation. A lot of focus has been on how surface discharges cause complete insulation failure

directly or in synergy with other various insulation ageing agents such as moisture [13]. There is however little literature on surface discharges and their possible influences on the LI withstand voltage of pressboard insulation in power transformers that specifically focus on the discharge magnitude.

Lightning and switching impulse endurance is an important design and performance parameter of power transformers. Colla et al [18] reported the degrading effect of repetitive switching impulses on oil-impregnated insulation in power transformer bushings. The insulation degradation was manifested by specific behavioural trends of the resulting partial discharge activity.

Studies of common failure modes of power transformers have revealed that lightning and switching transient voltages make up a significant portion of transformer failure modes. In South Africa, lightning and switching impulse voltages contribute about 12% to the total number of power transformer failures. Furthermore, lightning and switching voltage impulses contribute more than 50% of failures in the power rating category greater than 400 MVA [19-21]. Atmospheric conditions that are characterised by high altitudes in the order of 1700 m and high lightning ground flash density (10-15 flashes/km^2/year) as in South Africa [22] make lightning impulse voltages to be a major cause of transformer problems. It is therefore essential to understand and mitigate lightning impulse voltage failure as causes of transformer failure focusing on oil-impregnated pressboard.

As presented in detail in the rest of the paper, virgin samples of pressboard were dried under vacuum and then impregnated with dry mineral transformer oil. The samples were then exposed to surface discharges after which the lightning breakdown voltage was determined in comparison with control samples that had not been exposed to surface discharges. A conclusion was then drawn from the analysed test results.

3. THE EXPERIMENTAL PROCEDURE

3.1 Sample preparation and preconditioning

Controlled experimental studies on oil-impregnated pressboard typically entail preconditioning the pressboard material to ensure carefully controlled moisture levels and the degree of oil-impregnation. In the present work, the test samples' preconditioning processes were conducted at a power transformer manufacturing factory; Powertech Transformers Pty (Ltd), in South Africa. The pressboard sheets were 3 mm thick and each cut into square pieces of 100 mm x 100 mm. The pressboard samples were preconditioned and impregnated with oil in accordance with the IEC 60243-1 standard [23]. The samples were pre-dried in hot circulating air at 105 °C for 24 hours and then bathed in dry oil for 3 hours. The samples were then subjected to a vacuum-oven drying cycle in an autoclave at 130 °C for 48 hours. The oil impregnation was through emersion in dry oil under vacuum for a further 3 hours. The moisture content in the preconditioned pressboard was measured to be about 1,5%. The preconditioned samples were kept in an air tight container ready for the next stage of the experiment.

3.2 Electrode setup and partial discharge measurements

In order to expose the oil-impregnated pressboard test samples to surface discharges, a needle at an acute angle to plane electrode arrangement was used as shown in Figure 1, a setup devised by Mitchinson et al [16]. The resultant surface discharges were a function of the needle tip radius, insulation gap distance and the voltage across the insulation gap. For the needle tip radius of 0,117 mm used in this study, iterative tests were performed to determine the optimal gap setting and voltage magnitude that would produce sustained surface discharges for a sufficiently long period without flashover or puncture of the pressboard [24]. An electrode gap (d) of 45 mm and voltage of 30 kV_{rms} at 50 Hz were determined to be optimal for surface discharge ageing of the oil-impregnated pressboard.

Partial discharges on the pressboard were measured using a narrowband detection setup in accordance with the IEC 60270 standard [25] as shown in Figure 1. The PD measurement system was of the Power Diagnostics ICMCompact™ type. The setup was calibrated by injecting 10 pC from a calibrator connected across the test object. The experimental measurements were conducted in a shielded high voltage laboratory environment with an average noise level of 0,3 pC. The PD inception voltage (PDIV) was determined by slowly increasing the test voltage in steps of 1 kV until partial discharges above the noise threshold were detected. PD phase resolved patterns were recorded for 1 minute at the selected voltage level of 30 kV_{rms}.

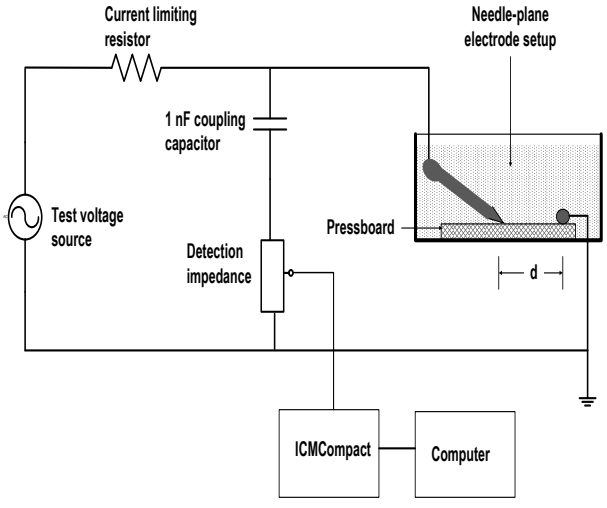

Figure 1: The partial discharge measurement setup showing the needle at an angle to ground electrode configuration on the oil-impregnated pressboard.

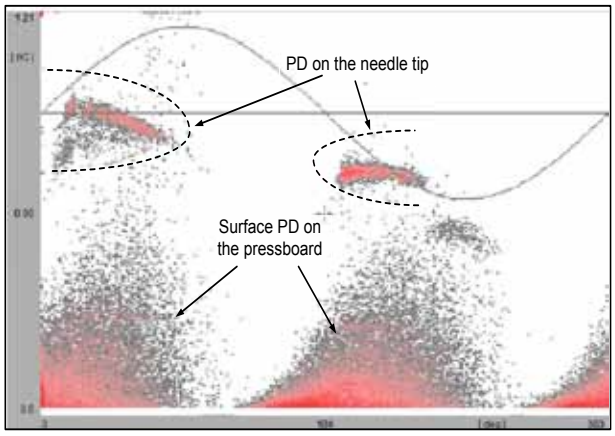

Figure 2: The recorded PD phase-resolved-pattern at 30 kV for the 45 mm electrode gap.

A typical PD phase-resolved-pattern recorded for the discharges on the pressboard is as shown in Figure 2. It is evident that the PD pattern manifests two sources of PD activity as labelled on the figure. The higher magnitude clusters in both half cycles (in the order of nC) are from the needle tip while the relatively smaller magnitude cluster (in the order of hundreds on pC) are those from the surface discharges along the tracks on the pressboard surface. The discharge distributions extend from the zero crossings into the first and third quarter regions which is typical for surface discharge pattern [16, 26]. In the absence of the pressboard, the epochs would have been concentrated around the voltage peaks as reported by Pompili et al [27]. It is also notable in Figure 2 that the average magnitudes of the surface discharges were below 500 pC.

The variations of the PD inception voltage (PDIV) and gap breakdown voltage of the oil/pressboard interface as a function of gap distance is shown in Figure 3. Below 25 mm, the gap broke down without prior PD inception. Beyond 25 mm the gap breakdown voltage increased linearly with increase in the gap size while the PDIV was statistically invariant. The manner in which the PDIV and electrode gap distance vary as a function of the electrode gap distance on the oil/pressboard interface is a characteristic of interest that has been investigated by many researchers.

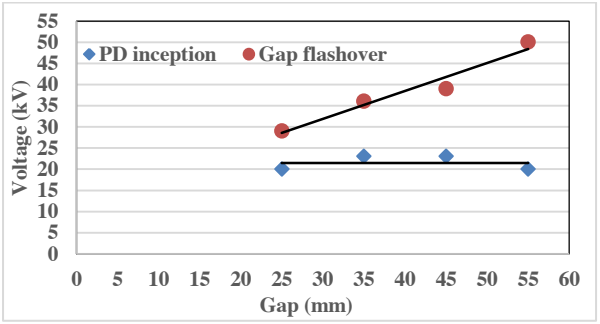

Figure 3: PDIV and gap flashover voltage as a function of gap length.

Dai et al [15] investigated the effect of moisture on the surface discharges on oil-impregnated pressboard using the same electrode setup as in Figure 1. The reported behavior of the PDIV and gap flashover voltage as a function of the gap distance was similar to that obtained in the present work given in Figure 3. It was also reported that for a given gap distance, the breakdown voltage of the oil gap was the same as that of the oil/pressboard interface which lead to a conclusion that if the pressboard surface is dry and clean, the presence of the pressboard does not influence the breakdown voltage of the oil gap. Furthermore in their work, it was found that in wet oil, the gap breakdown voltage was lower as an indication of the undesirable effect of moisture in transformer insulation [15].

Lv et al [28] investigated the effect of nanoparticles on creeping flashover characteristics on the oil/pressboard interface and reported the same behavioural trend as that of Figure 3. Most importantly they noted a significant shift in the PDIV and gap breakdown plots showing that the presence of the nanoparticle fillers in insulation oil increases the PDIV as well as the gap flashover voltage.

It can be suggested that the plots of gap flashover voltage and PDIV as a function of electrode gap distance for a needle-plane electrode setup on an oil/pressboard interface, typically give the same trends although the absolute values of the data points may vary slightly. The plots can therefore be suggested to be a conventional way of verifying the validity of test results obtained through similar experimental methodologies, and this is in agreement with Mitchnson et al [13].

It is also notable that in Figure 3 the PDIV is quasi-constant as the electrode gap increases. This is attributable to the fact that the partial discharges are initiated around the enhanced stress on the needle tip which, for relatively larger gaps, changes little as the gap increases. The maximum electric field (E_{max}) on the needle tip in a point-plane configuration can be analytically calculated using Equation (1) [29].

$$E_{max} = \frac{2V}{r ln\left(\frac{4d}{r}+1\right)} \quad (1)$$

Where:

V is the voltage across the insulation gap,
r is the needle tip radius,
d is the gap between the needle tip and the plane electrode.

At 30 kV and electrode gap distance of 45 mm, the maximum electric field on the needle tip is calculated to be 69.8 kV/mm using (1). Corresponding simulations in finite element method (FEM) field plot (as shown in Figure 4) give a value of 68 kV/mm which is practically the same as that determined analytically.

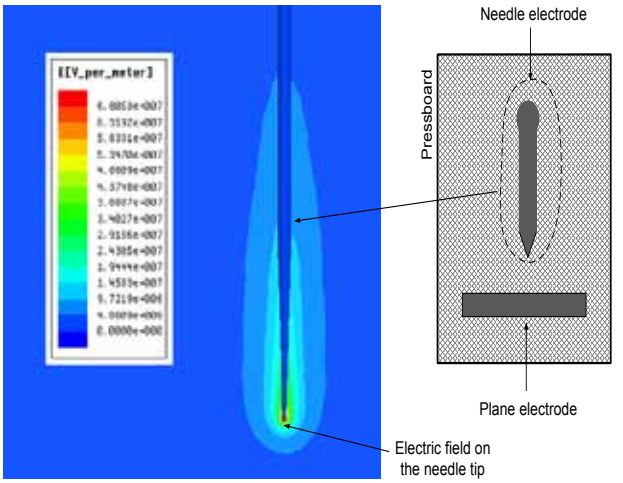

Figure 4: FEM electric field plot of the needle-plane electrode setup at gap distance of 45 mm and voltage of 30 kV showing the stress enhancement on the needle tip.

3.3 Surface discharge ageing of the oil-impregnated pressboard samples.

In order to simultaneously subject multiple samples of pressboard surface discharge to ageing at 30 kV_{rms}, the test sample setup in Figure 1 was duplicated to form an array of multi samples arranged in a transparent Perspex oil-filled tank as illustrated in Figure 5. To ensure that surface discharges occurred only on the desired regions of the test samples, copper tubes were used for the high voltage supply as well as for the grounded electrode. All needle connections to the high voltage supply were dimensioned to be free from corona at 30 kV_{rms}. The tank was covered with a Perspex transparent lid to limit ingress of moisture into the oil from the atmosphere and also enable visual inspection of the samples during the surface discharge ageing process.

One set of 12 of the oil-impregnated pressboard test samples was continuously exposed to surface discharges for a period of 3 hours after which they were removed and immediately subjected to the lightning voltage breakdown tests. Another set of 12 samples was exposed to surface discharges for a longer period of 7 hours after which they were also tested for lightning breakdown voltage.

Surface discharges on the oil-impregnated pressboard created tree shaped white tracks on the pressboard surface radiating from the needle tip and with time, extended towards the grounded electrode. An example is shown in Figure 6 for one of the samples exposed to 3 hours of surface discharge ageing. The white tree-shaped tracks are attributed to migration of oil and moisture out of the inter-fibre micro spaces on the pressboard surface layer under the influence of intense localized PD energy bombardment. The affected regions of the pressboard become effectively non-impregnated. Further stress enhancement ensues in the gas-filled microstructures and a runaway degradation process is initiated.

With prolonged PD activity, the white dendrite tracks turned into carbon tracks (black colour) as shown in Figure 7 due to physiochemical changes to the molecular matrix as PD energy continued to be injected.

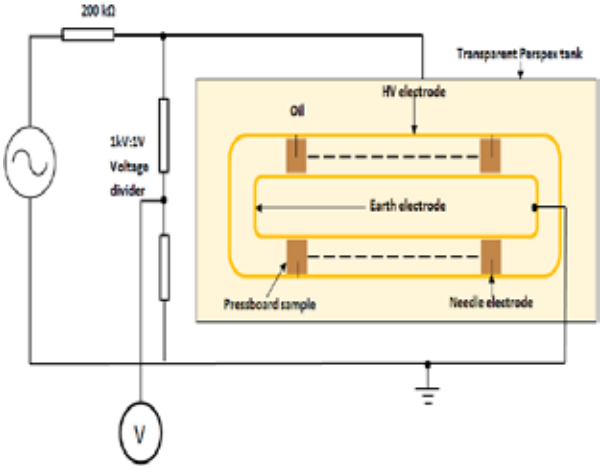

Figure 5: The multi-sample setup for surface discharge ageing of the oil impregnated pressboard.

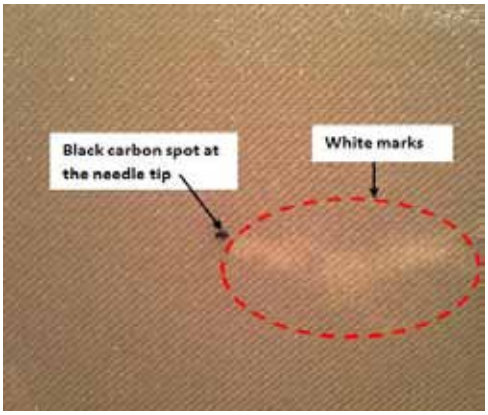

Figure 6: An example of a pressboard sample exposed to 3 hour surface discharge ageing showing the white track marks.

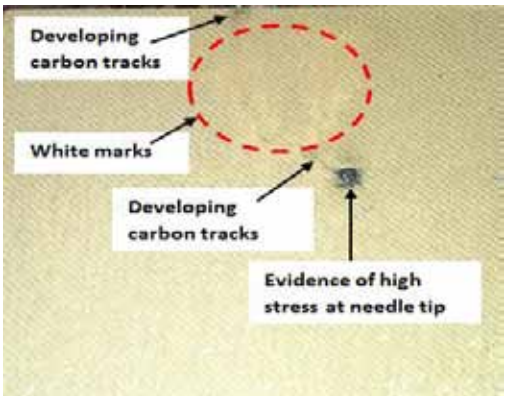

Figure 7: An example of a pressboard sample exposed to 7 hours of surface discharge ageing showing development of carbon traces.

3.4 Lightning impulse breakdown voltage tests of the surface-discharge-aged pressboard

The multilevel test method of breakdown tests was used in assessing the influence of surface discharges on the LI impulse voltage strength of oil-impregnated pressboard. The types of electrodes used are as shown in Figure 8 in accordance with IEC 60243-3 standard [30] and were immersed in oil during the breakdown tests to avoid spurious flashovers. The test voltage was a 1.3/54 μs lightning impulse from a multistage stage Marx generator.

The multilevel method of breakdown voltage test entails estimating the starting voltage magnitude, which should be 70% of the expected breakdown voltage for negative polarity and 60% for positive polarity. The voltage was incremented in steps and 3 shots applied at each voltage level. The sequence was repeated until breakdown. A 1-minute interval was allowed between successive shots to avoid the influence of space charge that would have been generated in the previous shot.

For the 3 mm thick pressboard samples used in this work and using the Equation (2) [31], the expected negative polarity lightning impulse breakdown voltage would be 223 kV.

$$E_b = \frac{94.6}{d^{0.22}} \quad (2)$$

Where;

d is the insulation thickness and E_b is the maximum breakdown strength of the insulation.

The starting voltage in the multilevel voltage test procedure was therefore chosen as 156 kV for the negative polarity impulses and 134 kV for the positive impulses. For each of the impulse voltage polarities, 3 sets of oil-impregnated pressboard samples were tested as follows:

- 9 samples of unaged pressboard as a control set,
- 6 samples of the 3-hour surface discharge aged,
- 6 samples of the 7-hour surface discharge aged.

The test results, analysis and discussion are presented in the next section.

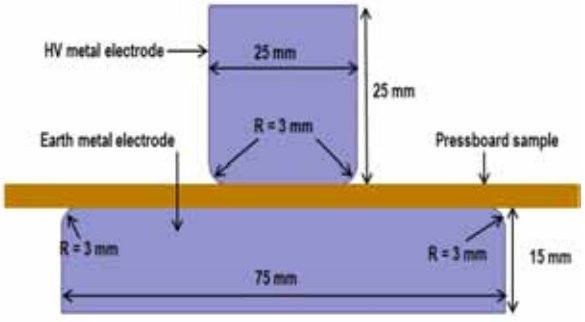

Figure 8: Details of the electrode setup for the lightning impulse voltage breakdown test in accordance with [30].

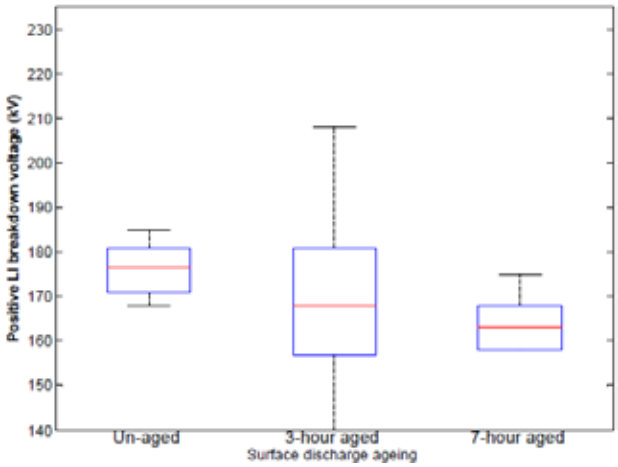

Figure 9: Boxplot of the positive lightning impulse voltage breakdown as a function of time of exposure of the pressboard to surface discharges.

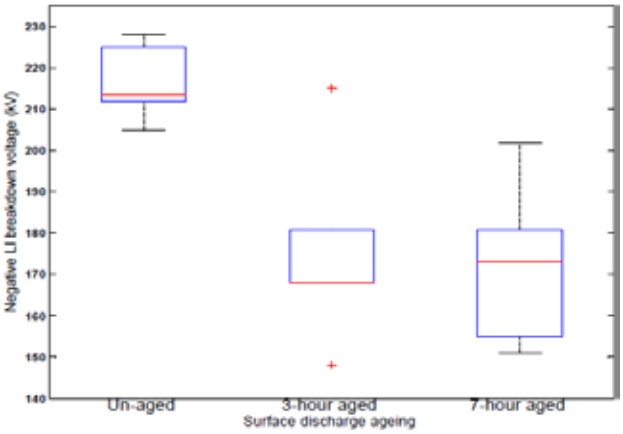

Figure 10: Boxplot of the negative lightning impulse voltage breakdown as a function of time of exposure of the pressboard to surface discharges.

4. RESULTS, ANALYSIS AND DISCUSSION

The lightning breakdown voltage test results of the aged and unaged oil-impregnated pressboard for positive and negative and polarity voltages are given in Tables 1 and 2 respectively. Figures 9 and 10 are the corresponding box plots presentations of the changes in the lightning breakdown voltage of the pressboard due to exposure to surface discharges. It is notable that exposure of oil-impregnated pressboard to surface discharges lowers the lightning breakdown voltage of the pressboard by about 15% for the negative polarity voltage and 4% for the positive polarity. These findings are consistent with similar results by Okabe et al [11] who concluded that the impulse voltage insulation strength of pressboard was reduced by about 30 % due to the exposure of the pressboard to partial discharges of at least 50 000 pC. They went on to conclude that the minimum harmful level of partial discharges in power transformers could be regarded as 10 000 pC, a magnitude 20 times bigger than the PD magnitudes measured in the present work. The

question of what surface PD magnitude is significant in reducing the LI impulse strength of oil impregnated pressboard is therefore not yet fully addressed.

As expected, the negative polarity lightning breakdown voltage was higher than that of the positive polarity. The difference is attributed to the classical theory of electrical breakdown mechanisms [32] as illustrated in Figure 11. Under positive polarity, electrons are attracted towards the anode and in the process cause ionization avalanches in the insulation medium. Each ionization avalanche event creates an anvil shaped 'cloud' of relatively slow moving positive ions with the broader end of the cloud facing the anode as shown in Figure 11a. Consequently the space-charge-distorted electric field around the avalanche head is greatly enhanced and making it relatively easier than in the negative polarity case for the ionization avalanches (streamers) to advance further into the insulation. In the negative polarity case, the orientation of the positive ion clouds is opposite to that of the positive polarity as shown in Figure 11b. The resultant space-charge-modified electric field on the avalanche head is not as greatly enhanced as in the positive polarity case. Consequently it requires higher negative polarity voltage to create the same breakdown effect as the positive polarity. This is consistent with the results obtained in the present work.

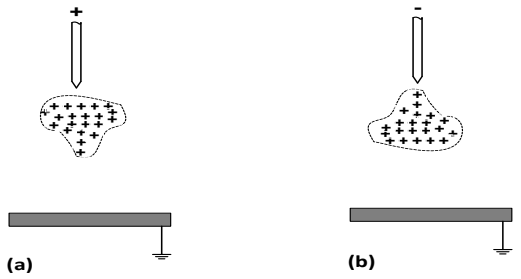

Figure 11: Sketches of ionic avalanche mechanisms illustrating different orientations of the positive ion clouds (a) positive polarity and (b) negative polarity.

Table 1: Positive polarity lightning impulse breakdown voltage results of unaged and surface discharge aged test samples.

Sample number	Un-aged LI breakdown voltage (kV)	3 hours aged LI breakdown voltage (kV)	7 hours aged LI breakdown voltage (kV)
1	155	128	158
2	165	157	158
3	165	168	158
4	168	168	168
5	171	181	168
6	175	208	175
7	178	-	-
8	181	-	-
9	185	-	-
Average breakdown voltage (kV)	**171**	**168**	**164**

Table 2: Negative polarity lightning impulse breakdown voltage results of unaged and surface discharge aged test samples.

Sample number	Un-aged LI breakdown voltage (kV)	3 hours aged LI breakdown voltage (kV)	7 hours aged LI breakdown voltage (kV)
1	175	148	151
2	178	168	155
3	185	168	165
4	205	168	181
5	212	181	181
6	212	215	202
7	215	-	-
8	225	-	-
9	228	-	-
Average breakdown voltage (kV)	**204**	**175**	**173**

It is also noticeable that the difference in the lightning breakdown voltage values of unaged and aged samples is much greater for the negative polarity (15%) than in the case of positive polarity (4%). Comparison of trends in Figures 9 and 10 show remarkable differences between positive and negative polarities in the extent to which the surface discharges change the lightning impulse breakdown voltage of the oil-impregnated pressboard. At this stage there is no available explanation of the difference in the effect of surface discharges being more pronounced with negative polarity than positive polarity LI voltages, and this may be a subject of future studies.

It is a common practice to use Weibull analysis techniques in the analysis of electrical breakdown tests results [33]. In that regard Figure 12 further illustrates the marked difference between negative polarity and positive breakdown voltages.

In Figure 13 the Weibull plot for the negative polarity case gives clearer visual impression of the extent to which lightning breakdown voltage of oil-impregnated pressboard is reduced by exposure to surface discharges.

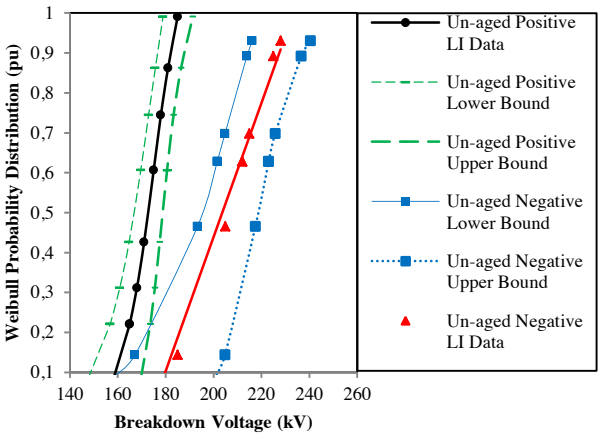

Figure 12: 95% confidence bound Weibull plot for unaged negative and positive lightning breakdown voltage.

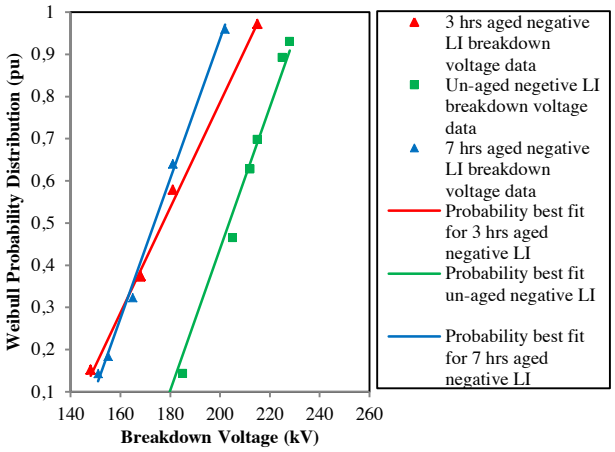

Figure 13: 95% confidence bound Weibull plot for unaged negative and positive lightning breakdown voltage.

5. CONCLUSION

Surface discharge of magnitude in the order of some hundreds of pC reduces the lightning impulse breakdown strength of oil-impregnated pressboard in power transformers. Although the negative polarity LI withstand voltage of surface discharge-aged pressboard is higher than that of positive polarity, the reduction in the LI voltage strength is more pronounced for the negative LI impulse voltage. The findings suggest further scrutiny of standardised acceptable magnitudes of partial discharges in power transformers.

ACKNOWLEDGEMENT

The authors wish to acknowledge Eskom and the National Research Foundation (NRF) for their continued support of the high voltage engineering research work at the University of the Witwatersrand, Johannesburg. Powertech Transformers (Pty) Ltd. is greatly acknowledged for their various contributions to this research work.

REFERENCES

[1] R. Bartnikas, "Partial Discharges: Their Mechanism, Detection and Measurement" *IEEE Transactions on Dielectrics and Electrical Insulation,* Vol. 9, No.5, pp.763-808, 2002.

[2] J. Fuhr, "Procedure for Identification and Localisation of Dangerous PD Sources in Power Transformers", *IEEE Transactions on Dielectrics and Electrical Insulation,* Vol. 12, No. 5, pp. 1005-1014, 2005.

[3] Z. Tang, C. Li, X. Cheng, W. Wang, and J. Li, "Partial Discharge Location in Power Transformers Using Wideband RF Detection", *IEEE Transactions on Dielectrics and Electrical Insulation*, Vol. 13, No. 6, pp. 1193-1193, 2006.

[4] S.M. Markalous, S. Tenbohlen and K. Feser, "Detection and Location of Partial Discharges in Power Transformers Using Acoustic and Electromagnetic Signals", *IEEE Transactions on Dielectrics and Electrical Insulation,* Vol. 15, No. 6, pp. 1576-1583, 2008.

[5] S. Meijer, P.D. Agoris, J.J. Smit, M.D. Judd and L. Yang, "Application of UHF Diagnostics to Detect PD During Power Transformer Acceptance Tests", *IEEE International Symposium on Electrical Insulation,* Toronto, Canada, 2006.

[6] F. Marangoni, J.P. Reynders and P.J. de Klerk, "Investigating into the Effects of Different Antenna Dimensions for UHF Detection of Partial Discharges in Power Transformers", *IEEE Power Tech Conference,* Bologna, Italy, June 23-26, 2003.

[7] S. Meijer, M.D. Judd and S. Tenbohlen, "Sensitivity Check for Radio Frequency Partial Discharge Detection of Power Transformers", *International Conference on Condition Monitoring and Diagnosis,* Beijing, China, April 2008.

[8] A.S. Kumar, R.P. Gupta, K. Udayakumar and A. Venkatasami, "Online Partial Discharge Detection and Location Techniques for Condition Monitoring of Power Transformers: A Review", *International Conference Condition Monitoring and Diagnosis,* Beijing, China, Aril 21-24, 2008.

[9] IEC 60076-3, Power Transformers Part 3: Insulation levels, dielectric tests and external clearances in air, *IEC Standard*, 2000.

[10] IEC 60076-3, Power Transformers Part 3: Insulation levels, dielectric tests and external clearances in air, *IEC Standard,* 2013.

[11] S. Okabe, G. Ueta, H. Wada and H. Okubo, "Partial Discharge-induced Degradation Characteristics of Insulating Structure Constituting Oil-immersed Power Transformers", *IEEE Transactions on Dielectrics and Electrical Insulation,* Vol. 17, No. 5, pp. 1649-1656, 2010.

[12] S. Okabe, G. Ueta, H. Okubo, "Partial Discharge-induced Degradation Characteristics of Oil-impregnated Insulating Material Used in Oil-immersed Transformer Insulation", *IEEE Transactions on Dielectrics and Electrical Insulation,* Vol. 17, No. 5, pp. 1473-1480, 2010.

[13] P.M. Mitchnson, P.L. Lewin, B.D. Strawbridge and P. Jarman, "Tracking and Surface Discharge at the Oil-Pressboard Interface", *IEEE Electrical Insulation Magazine,* Vol. 26, No.2, pp. 35-41, 2010.

[14] W. Wang, Y. Xue, Y. Cheng, B. Zhou, J. Xu and C. Li, "Diagnosis of Severity Degree for Oil/pressboard Insulation Surface Discharge", *IEEE Annual Report Conference on Electrical Insulation and Dielectric Phenomena (CEIDP2011),* Cancun, Mexico, 2011.

[15] J. Dai, Z.D. Wang, and P. Jarman, "Moisture and Aging Effect on the Creepage Discharge Characteristics at the Oil/Transformer-board Interface under Divergent Field", *IEEE Annual*

Report Conference on Electrical Insulation and Dielectric Phenomena (CEIDP), Québec City, Canada, 2008.

[16] P.M. Mitchinson, P.L. Lewin, G. Chen and P.N. Jarman, "A new Approach to the Study of Surface Discharge on the Oil-Pressboard Interface", *IEEE International Conference on Dielectric Liquids (ICDL),* Poitiers, France, pp. 186-189, 2008.

[17] H.Z. Ding, Z.D. Wang, and P.N. Jarman, "Effect of Ageing on the Impulse Breakdown Strength of Oil-impregnated Pressboard Used in Power Transformers", *IEEE Annual Report Conference on Electrical Insulation and Dielectric Phenomena (CEIDP),* Kansas City, MO, USA, 2006.

[18] F. Colla, M. Pompili, C. Mazzetti, U. Ratti and R. Bartnikas, "Aging of Dielectric Liquid-Impreganted-Paper Insulated Bushings Under Voltage Switching Surges", *Proceedings of the 13th International Conference on Dielectric Liquids (ICDL'99),* Nara, Japan, pp. 414-417, July 1999.

[19] M. Minhas, J.P. Reynders and P.J. de Klerk, "Failure in Power System Transformers and Appropriate Monitoring Techniques", *Proceedings of the 11th International Symposium on High Voltage Engineering (ISH),* London, U.K. 1999.

[20] A.K. Lokhanin, G.Y. Shneider, V.V. Sokolov, V.M. Chornogotsky and T.I. Morozova, "Internal Insulation Failure Mechanisms of HV Equipment Under Service Conditions", *Cigré Paris Session,* 2002, paper no.15-201.

[21] M. Wang, A.J. Vandermaar and K.D. Srivastava, "Review of Condition Assessment of Power Transformers in Service", *IEEE Electrical Insulation Magazine,* Vol. 18, Issue 6, pp. 13-25, 2002.

[22] M. Gijben, "The Lightning Climatology in South Africa", *South African Journal of Science,* 108(1/4), pp. 1-10, 2012.

[23] IEC 60243-1, Electrical Strength of Insulating Material – Test Method, Part 1: Testing at Power Frequency, *IEC Standard,* Second Edition, 1998.

[24] M.M. Tshivhilinge, "A Comparative Study on the Effect of Surface Discharges on the Impulse Breakdown Voltage of Oil-Impregnated Pressboard Insulation", *MSc Dissertation,* University of the Witwatersrand, Johannesburg, pp.37-45, 2014.

[25] IEC 60270-2000, High-voltage Test Techniques – Partial Discharge Measurements.

[26] M.G. Niasar, "Partial Discharge Signatures of Defects in Insulation Systems Consisting of Oil and Oil Impregnated Paper", *Licentiate Thesis,* KTH School of Electrical Engineering, Stockholm, Sweden, 2012.

[27] M. Pompili, C. Mazzetti and R. Bartnikas, "Phase Relationship of PD Pulses in Dielectric Liquids under ac Conditions", *IEEE Transactions on Dielectrics and Electrical Insulation,* Vol. 7, No. 1, pp. 113-117, 2000.

[28] Y.Y. Lv, Y. Zhou, C.R. Li, K.B. Ma, Q. Wang, W. Wang, S.N. Zhang and Z.Y. Jin, "Nanoparticle Effects on Creeping Flashover Characteristics of Oil/Pressboard Interface", *IEEE Transactions on Dielectrics and Electrical Insulation,* Vol. 21, No. 2, pp. 556-559, 2014.

[29] J.H. Mason, "Breakdown of Solid Dielectrics in Divergent Fields", *Monograph No. 127M, British Electrical and Allied Industries Research Association,* pp. 254-263, 1955.

[30] IEC 60243-3, Electrical Strength of Insulating Material - Test Method, Part 3: Additional Requirements for 1,2/50 μs Impulse Tests, Second Edition, *IEC Standard,* 2001.

[31] R.M. Del Vecchio, B. Poulin, P. T. Feghali, D.M. Shah and R. Ahuja, *Transformer Design Principles with Applications to Core-Form Power Transformers,* Second Edition, CRC Press, 2010, Chapter 13.

[32] E. Kuffel, W.S. Zaengl and J. Kuffel, *High Voltage Engineering Fundamentals,* Butterworth-Heinemann, U.K. 2nd Edition, pp. 348-359, 2000.

[33] IEEE Guide; Statistical Analysis of Electrical Insulation Breakdown Data, *IEEE 930TM,* First Edition, 2007.

NOTES

SAIEE AFRICA RESEARCH JOURNAL – NOTES FOR AUTHORS

This journal publishes research, survey and expository contributions in the field of electrical, electronics, computer, information and communications engineering. Articles may be of a theoretical or applied nature, must be novel and must not have been published elsewhere.

Nature of Articles

Two types of articles may be submitted:

- Papers: Presentation of significant research and development and/or novel applications in electrical, electronic, computer, information or communications engineering.
- Research and Development Notes: Brief technical contributions, technical comments on published papers or on electrical engineering topics.

All contributions are reviewed with the aid of appropriate reviewers. A slightly simplified review procedure is used in the case of Research and Development Notes, to minimize publication delays. No maximum length for a paper is prescribed. However, authors should keep in mind that a significant factor in the review of the manuscript will be its length relative to its content and clarity of writing. Membership of the SAIEE is not required.

Process for initial submission of manuscript

Preferred submission is by e-mail in electronic MS Word and PDF formats. PDF format files should be 'press optimised' and include all embedded fonts, diagrams etc. All diagrams to be in black and white (not colour). For printed submissions contact the Managing Editor. Submissions should be made to:

The Managing Editor, SAIEE Africa Research Journal,
PO Box 751253, Gardenview 2047, South Africa.
E-mail: researchjournal@saiee.org.za

These submissions will be used in the review process. Receipt will be acknowledged by the Editor-in-Chief and subsequently by the assigned Specialist Editor, who will further handle the paper and all correspondence pertaining to it. Once accepted for publication, you will be notified of acceptance and of any alterations necessary. You will then be requested to prepare and submit the final script. The initial paper should be structured as follows:

- TITLE in capitals, not underlined.
- Author name(s): First name(s) or initials, surname (without academic title or preposition 'by')
- Abstract, in single spacing, not exceeding 20 lines.
- List of references (references to published literature should be cited in the text using Arabic numerals in square brackets and arranged in numerical order in the List of References).
- Author(s) affiliation and postal address(es), and email address(es).
- Footnotes, if unavoidable, should be typed in single spacing.
- Authors must refer to the website: http: //www.saiee.org.za/arj where detailed guidelines, including templates, are provided.

Format of the final manuscript

The final manuscript will be produced in a 'direct to plate' process. The assigned Specialist Editor will provide you with instructions for preparation of the final manuscript and required format, to be submitted directly to:
The Managing Editor, SAIEE Africa Research Journal, PO Box 751253, Gardenview 2047, South Africa.
E-mail: researchjournal@saiee.org.za

Page charges

A page charge of R200 per page will be charged to offset some of the expenses incurred in publishing the work. Detailed instructions will be sent to you once your manuscript has been accepted for publication.

Additional copies

An additional copy of the issue in which articles appear, will be provided free of charge to authors.
If the page charge is honoured the authors will also receive 10 free reprints without covers.

Copyright

South African Institute for Electrical Engineers (SAIEE)
PO Box 751253, Gardenview, 2047, South Africa
Tel: 27 11 487 3003 | Fax: 27 11 487 3002
E-mail: researchjournal@saiee.org.za | Website: www.saiee.org.za